AMIDR: A COMPLETE PULSE METHOD FOR MEASURING SOLID-STATE DIFFUSIVITY IN LI-ION CELLS

by

Mitchell A. Ball

Submitted in partial fulfilment of the requirements

for the degree of Master of Science

at

Dalhousie University

Halifax, Nova Scotia

November 2023

Table of Contents

List of Tables

List of Figures

Abstract

The Atlung Method for Intercalant Diffusion and Resistance (AMIDR) is a novel, high accuracy method for measuring solid state diffusivity and cell internal resistance related to the Atlung Method for Intercalant Diffusion (AMID) with several key differences. Most notably, AMIDR is designed to analyze the voltage response over time of "complete" pulses, pulses that last until an impedance steady state is reached. These differences, in addition to design considerations made when designing AMID, allow for AMIDR to return diffusivity results with a higher degree of confidence than Galvanostatic Intermittent Titration Technique (GITT) and at a faster rate with higher state of charge (SOC) resolution than Electrochemical Impedance Spectroscopy (EIS). In this study, three different, commercial, layered lithium transition metal oxides were studied. These active materials showed very similar kinetic behaviour that varied quantitatively with dependence on the fraction of Ni atoms filling sites in the Li layer. AMIDR comes with a user-friendly python program that is intended to assist other researchers in measuring active material diffusivity with the same degree of accuracy in a controlled, repeatable manner. This program, along with instruction on its use, the results of this study from raw data to the final key kinetic metrics, and a video summary of AMIDR design are available for download at https://github.com/MitchBall/AMIDR.

List of Abbreviations and Symbols Used

AC	Alternating Current
AMID	Atlung Method for Intercalant Diffusion
AMIDR	Atlung Method for Intercalant Diffusion and Resistance
CC	Constant Current
DMC	Dimethyl Carbonate
EC	Ethyl Carbonate
EIS	Electrochemical Impedance Spectroscopy
FEM	Finite Element Method
GITT	Galvanostatic Intermittent Titration Technique
LFP	$LiFePO_4$
LMFP	$LiMn_{1-x}Fe_xPO_4$
LMO	$LiMn_2O_4$
LTO	$Li_{4/3}Ti_{5/3}O_4$
NMC	$LiNi_{1-x-y}Mn_xCo_yO_2$
NMCA	$LiNi_{1-x-y-z}Mn_xCo_yAl_zO_2$
NMP	N-Methyl-2-pyrrolidone
PVDF	Polyvinylidene Fluoride
SEI	Solid Electrolyte Interphase
SEM	Secondary Electron Microscopy
SOC	State of Charge
XRD	X-ray Diffraction
a	distance between two occupation sites (cm)
A	geometric constant (1 for a planar sheet, 2 for a cylinder, 3 for a sphere)
α_i	series of geometric constants defined by equations
B	geometric constant (3 for a planar sheet, 4 for a cylinder, 5 for a sphere)
c	ion concentration (mol cm^{-3})
c_s	surface c (mol cm^{-3})
c_{sat}	c of a completely saturated active material (mol cm^{-3})
Δc	change in c after a certain Δt (mol cm^{-3})
Δc_s	change in c_s after a certain Δt (mol cm^{-3})

$\Delta c_{s,loss}$	deviation in c_s from impedance-free scenario (mol cm^{-3})
Δc_{tot}	change in c if n_{tot} moles are evenly transported (mol cm^{-3})
C	dimensionality constant
$C(\alpha, z)$	geometric function
dE/dc	relationship between c and E at any given SOC
dq/dV	relationship between V and q at any given SOC
D_c	chemical diffusivity (cm^2 s^{-1})
$D_{c,s}$	surface D_c (cm^2 s^{-1})
D_t	tracer diffusivity (cm^2 s^{-1})
D_t^*	free-path tracer diffusivity (cm^2 s^{-1})
∇D_c	spatial gradient of D_c (cm s^{-1})
$\nabla \widetilde{D}_c$	relative spatial gradient of D_c (cm^{-1})
$\nabla \widetilde{D}_{c,s}$	surface relative spatial gradient of D_c (cm^{-1})
E	electrode potential (V)
E_c	counter E (V)
E_w	working E (V)
F	Faraday's constant (C mol^{-1})
ΔG_A	occupation site hop activation energy (J)
I	applied current (A)
I_c	critical I that triggers end of discharge runaway feedback loop (A)
I_j	I of an individual particle (A)
J	ionic flux (mol s^{-1} cm^{-2})
J_1	Bessel function of the first kind of order 1
k_B	Boltzmann constant (J K^{-1})
m	active material mass (g)
M	active material constant for describing D_c vs. c at low SOC (cm^2 s^{-1})
n	moles of ions transported after a certain Δt (mol)
N	active material constant for describing D_c vs. q at low SOC (cm^3 mol^{-1})
n_{tot}	moles of ions desired to be transported (mol)
N_A	Avogadro constant (mol^{-1})

P	relative resistance
q	capacity (C)
q_e	elementary charge (C)
q_{sat}	theoretical q of a fully saturated active material (C)
Δq	change in q after a certain Δt (C)
Δq_j	Δq of an individual particle (C)
Δq_c	cumulative change in q of a series of pulses (C)
Δq_i	ideal, impedance-free change in q corresponding to ΔV (C)
Δq_{tot}	change in q if n_{tot} moles are transported (C)
Δq_0	change in q after a pulse and relaxation (C)
Q	relative D_c
r	diffusion length or radius (cm)
r_j	r of an individual particle (cm)
$\bar{r}$	capacity-weighted geometric mean of r (cm)
$\bar{r}_e$	average r for modeling end of pulse (cm)
$\bar{r}_s$	average r for modeling start of pulse (cm)
R	resistance (Ω)
$R_{D,term}$	terminal diffusive R (Ω)
R_i	interface R (Ω)
R_{ohm}	combined electrical contact R and ionic electrolyte R (Ω)
S	electrode surface area (cm^2)
S_j	S of an individual particle (cm^2)
t	time (s)
Δt	pulse time (s)
T	temperature (K)
V	cell voltage (V)
ΔV	change in V after a certain Δt (V)
ΔV_i	ideal ΔV in an impedance-free scenario (V)
ΔV_{tot}	ΔV if n_{tot} moles are transported and active material allowed to relax (V)
ΔV_0	change in V after a pulse and relaxation (V)

ΔV_1	initial ΔV at start of pulse (V)
$\tilde{V}$	electrode volume (cm^3)
$\tilde{V}_j$	$\tilde{V}$ of an individual particle (cm^3)
X	relative Δc
X_s	relative Δc_s
$X_{s,loss}$	deviation in X_s from impedance-free scenario
$X_{s,ideal}$	ideal X_s under an impedance-free scenario
y	relative position along diffusion path
Y	relative ΔV
z	ion charge number
γ	activity coefficient
η	overpotential (V)
η_D	diffusion η (V)
η_R	resistance η (V)
μ	chemical potential ($J\ mol^{-1}$)
μ_0	intrinsic chemical potential ($J\ mol^{-1}$)
ν	vibrational frequency (s^{-1})
ρ_c	interface contact resistivity ($\Omega\ cm^2$)
ρ_d	active material density ($g\ cm^{-3}$)
τ	relative Δq

Acknowledgements

I would like to first thank my supervisor, Jeff Dahn, for his help, support, and rigorous and challenging discussions. It has been said before, but his dedication to students at seemingly all hours of the day is unique and inspirational. Secondly, I would also like to thank my unofficial supervisors, Chongyin Yang and Micheal Metzger for their insight, and our official lab manager, Michel B. Johnson, for fixing everything that myself or others may or may not have broke and training us so that it doesn't break again.

I also want to thank Marc Cormier, Eniko Zsoldos, and Nuttaphon Phattharasupakun for introducing me to my project and laying the groundwork for excellent Li-ion solid-state diffusivity measurements. In addition to those three, I also wish to thank Ines Haman, Svena Yu, Ning Zhang, Libin Zhang, and Bailey Rutherford for sharing some of their data.

Lastly, I wish to thank all members of the Dahn lab for providing such a cooperative and enjoyable environment for the research of battery design.

Chapter 1: Introduction

1.1 Motivation

Li-ion batteries are energy storage devices used in many products like portable consumer electronics such as phones and laptops, vehicles ranging from drones to buses, and occasionally stationary grid energy storage. These batteries have many different performance metrics including cycle life, self discharge rate, power density, and energy density. A good understanding of battery kinetic behaviour is necessary to improve power density and even energy density if cell capacity is kinetically hindered.[1] Power and energy density are limited by impedance which can come from many different parts of the cell. One common source is the active material at one of the two cell electrodes which produces interface resistance when Li^+ travels across its surface and solid-state diffusion impedance when Li^+ transports within its bulk.

There are many ways to measure these two active material impedances, but many of these methods suffer from a lack of repeatability, especially methods for diffusion impedance. Different studies have published diffusivity values that differ from each other by multiple orders of magnitude for the same material. Some studies even show a wide deviation between the values acquired by charging and discharging the same cells.[2] This shows that there is ample room for improvement when it comes to measuring diffusivity and a need for a new, easy-to-use method with better repeatability.

1.2 Scope

This thesis proposes and demonstrates a new method for accurately measuring diffusivity and interface resistance called the Atlung Method for Intercalant Diffusion and Resistance (AMIDR) that comes paired with an accessible Python program to encourage adoption. The materials measured within this thesis are all lithium nickel manganese cobalt (NMC) layered oxide cathode active materials which are commonly spherically shaped and have kinetically hindered capacities. However, this method may be applied to other active materials, both cathode and anode, and even other transport ions such as Na^+ or K^+, with appropriate modification.

Chapter 2 introduces the components of a Li-ion cell and Chapter 3 goes in depth on the mathematics behind modeling diffusivity. Chapter 4 provides background on prior methods used to measure diffusivity and the challenges they face using theory from the previous chapter. Chapter 5 defines AMIDR and the design considerations used for its construction whereas Chapter 6 provides the experimental parameters used for measuring active material within this thesis. Chapter 7 provides the results of the active materials studied and insight into their mechanisms of diffusion and Chapter 8 takes these discovered mechanisms and models their impact on typical cell performance. Chapter 9 summarizes and concludes this work and Chapter 10 provides future avenues of exploration and development for AMIDR. Portions of Chapters 3-7 and 9 will appear in the peer reviewed article: AMIDR: A Complete Pulse Method for Measuring Cathode Solid-State Diffusivity by M. Ball, M. Cormier, E. Zsoldos, I. Haman, S. Yu, N. Zhang, N. Phattharasupakun, M. B. Johnson, M. Metzger, C. Yang, and J. R. Dahn, submitted to the Journal of the Electrochemical Society.

Chapter 2: Li-ion Batteries

2.1 Li-ion Cell

Figure 1 shows a general schematic of a Li-ion cell during discharge. Li-ion cells comprise of two electrodes, an anode and a cathode, with a separator between them and electrolyte wetting all components. Typical battery convention will label an anode as the electrode with lower potential and the cathode as the electrode with higher potential contrary to the traditional definition of anodes and cathodes which define them as the electrodes undergoing oxidation and reduction respectively. Both electrodes consist of active material which stores electrons and lithium ions and is coated upon an electrically conductive current collector. Conversely, the electrolyte within the separator connecting the electrodes is ionically conductive but electrically insulative. These components are all sealed within the battery with the current collectors in electrical contact with external terminals. Typically, within a commercial battery, these components are all very thin and stacked upon each other with the current collectors coated upon both sides.

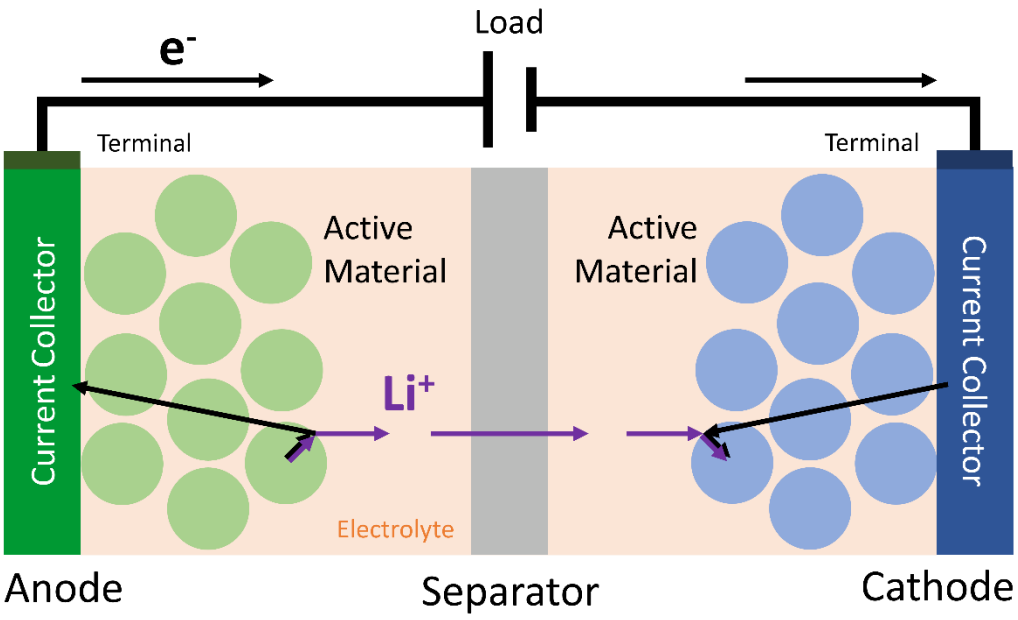

Figure 1: Schematic of a Li-ion cell during a discharge.

When the terminals are connected to a load, both ions and electrons begin to transport. Initially, the ions and electrons travel together from the bulk to the surface of the anode active material where they separate. The electrons conduct through the anode current collector to the load where they do work and then through the cathode current collector to the cathode active material. Conversely, the ions stay within the cell and travel through the electrolyte and separator until they reach the cathode active material as well. From there, the ions and electrons travel together again to the interior of the cathode active material. One caveat to this process is that if the load has a higher voltage than the difference in the resting potentials of the electrode, the load becomes a power source, this process will proceed in reverse, and the cell will charge. Typically, with completely reversible reactions, the difference in potentials between the electrodes will grow during charge and shrink during discharge.

Because the ions and electrons are paired when they are within the active material, there is no electric field to promote transport. Therefore, the remaining method of transport is diffusion. Because ions are far heavier and larger particles than electrons this transport is primarily limited by ion diffusion in layered oxides and the impact of electron diffusion is negligible.

2.2 Electrodes

Active material is typically coated to the current collectors with a small portion of binder like polyvinylidene fluoride (PVDF) and conductive additive like carbon black. However, some active materials like graphite will not require conductive additive as they are already electrically conductive.[3] Some common Li-ion cathode materials include $LiNi_{1-x-y-z}Mn_xCo_yAl_zO_2$ layered oxides (NMC/NMCA), $LiMn_{1-x}Fe_xPO_4$ (LMFP/LFP), and $LiMn_2O_4$ (LMO). The most common Li-ion anode material is graphite, but alternatives include Si-based active material (which is often mixed with a certain amount of carbon for stability), $Li_{4/3}Ti_{5/3}O_4$ (LTO), and lithium metal. Lithium metal is unique in that it does not require diffusion transport within the active material because there is no host material. Lastly, while only used in research settings, some cells have a third electrode called a reference electrode. This electrode is typically not coated on a flat current collector but coated on a mesh or a thin wire to allow ions to transport past it. Current is not drawn through this electrode, so it experiences no overpotential and can be used to determine the potential of other electrodes without convolution from the counter electrode overpotential. A common reference electrode is LiAu alloy although cathode and anode active materials can be used as well.[4]

Some active materials like LFP, LTO, and lithium metal have a single potential that ranges over all states of charge (SOC) and appears as a "plateau" when plotted. These plateaus are associated with discrete phase transitions. Other active materials like LMFP, LMO, and LiAu have a series of plateaus associated with a series of discrete phase transitions. Lastly, some materials like NMC/NMCA, graphite, and Si-based active material, have smaller plateaus which may be due to discrete or continuous phase transitions but also have wide ranges of potentials over varying SOC associated with continuous phase transitions. These potential ranges are not only dependent on the chemistry, but also variations in stoichiometry, both structural and dopant defects, and even morphology.[5,6] However, lithium metal is again unique as it has a consistent potential not dependent on these variations making it an excellent counter electrode for studying other materials. When lithium metal is used as a counter electrode this is referred to as a half cell as opposed to a full cell for any other arrangement.

Most active materials have a generally spherical shape, but internal ion transport pathways may have a more cylindrical or planar shape depending on the internal lattice. Diffusion transport through an active material introduces an impedance. The active materials used in this thesis are NMC at the cathode, lithium metal at the anode, and LiAu as a reference electrode.

2.3 Electrolyte

The electrolyte's main function is to allow ionic conduction from electrode to electrode while inhibiting electronic conduction. Typically, the electrolyte is an aqueous

or non-aqueous liquid salt solution containing the transport ion. Common Li-ion non-aqueous solvents are organic carbonates such as ethylene carbonate (EC) and dimethyl carbonate (DMC) and a common salt is $LiPF_6$.[3] Electrolyte is desired to be ionically conductive to reduce ionic resistance between the two active electrodes. Electrolytes must also remain stable at both electrodes or decompose in a predictable, controlled manner.

2.4 Electrode/Electrolyte Interface

At low potentials at the anode interface, electrolyte often reduces and ionically bonds with transport ions to form a thin, insoluble film called a solid-electrolyte interphase (SEI). This SEI is desired to be chemically stable and adhere well to the anode active material so as not to dissolve or flake off and produce more SEI which consumes additional electrolyte and lithium reducing capacity and cycle life. Commercially, it is typical that a variety of additives are also dissolved in the electrolyte to be reduced at the anode to produce a more stable SEI.

At high potentials at the cathode surface, oxidation often occurs which removes material rather than depositing it. Oxygen contained in the cathode active material may oxidize to produce O_2 which oxidizes the electrolyte to produce H_2O and CO_2.[7] This may also be in combination with loss of transition metal cations such as Mn, Fe, Ni, or Co. In NMC/NMCA materials, this may lead to a separate surface phase called a reconstructed surface layer.[8]

Both the SEI and the reconstructed surface layer may introduce an interface resistance. If neither of these surface phases are present, resistance will still exist in the

form of charge transfer resistance related to the reaction transferring Li^+ from an electrolyte solvation shell to the active material which can be deemed an interface resistance as well. In addition, the interfaces also develop a double layer with a certain capacitance which acts in parallel with the interface resistance if it is produced by the SEI, reconstructed surface layer, or charge transfer reaction.

2.5 Separator

The separator is used to physically isolate the electrodes from another so that they cannot electrically conduct with one another. This usually takes the form of a thin, porous polypropylene or polyethylene film. This porous film allows for ions to transport through. Ideally this film is as thin and porous as possible to minimize ionic resistance, but the separator must remain mechanically stable as well.

2.6 Circuit Modeling

Figure 2 shows two circuit model representations of the cathode within a Li-ion cell. Figure 2a is constructed with the electrolyte to the left, the current collector to the right, and the electrode-electrolyte interface in the center. The electrode-electrolyte interface forms a double layer which forms a capacitance (C_{dl}) and a current dependent potential difference (E_{dl}), the electrolyte contributes a resistance (R_{ion}) from ion transport, and the current collector as well as the conductive additive in the electrode contributes a resistance (R_{el}).

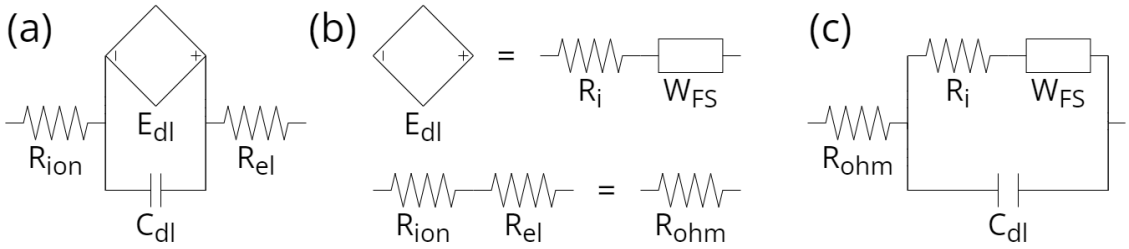

Figure 2: Circuit diagram of (a) a cathode with nodes corresponding to physical locations, (b) equivalent circuit elements, and (c) the Randle's circuit.

E_{dl} is dependent on the ion concentration at the active material surface and the charge transfer reaction, so it has a complex kinetic response. The charge transfer reaction will produce a current-overpotential relationship that follows the Butler-Volmer equation which simplifies to a simple resistance at low overpotentials (< 25 mV), so it is often expressed as such. If there is any resistive surface phase this will also be included with the charge transfer resistance as interface resistance (R_i). The concentration at the surface of the active material will be dependent on ion diffusion and produces a current-overpotential relationship described as a Warburg impedance. There are different variations of Warburg impedance and the one most accurately describing active material is the finite space Warburg impedance (W_{FS}) which evolves into a capacitance at long timescales that can maintain a potential at rest. However, at short timescales, all Warburg impedances act the same, so W_{FS} is sometimes simplified to a standard Warburg impedance which has no variation at long timescales and cannot maintain a potential at rest. As R_{ion} and R_{el} are two resistances in series they can be simplified to a single ohmic resistance (R_{ohm}).

These translations shown in Figure 2b can be applied to develop Figure 2c, a common representation of electrode impedance known as the Randle's circuit. While individual nodes within the Randle's circuit do not correspond to any physical locations

within or around the electrode, the entire circuit can be used to model the impedance of an electrode. If a standard Warburg impedance is selected, then the potential produced by the double layer will not be contained within the circuit, but this does not impact its ability to model overpotential. An anode model is nearly the same except the polarity of E_{dl} is reversed. A full cell model can be generated by mirroring an anode model and connecting it in series with a cathode model and combining R_{ion} or R_{ohm}.

Chapter 3: Diffusion Theory

When a current is applied to a Li-ion cell, lithium ions are transported from the electrolyte to the surface of an active material or vice versa at a certain flux. Transport within the active material from the surface to the interior and vice versa relies on solid-state diffusion. This diffusion is driven by lithium concentration gradients transporting lithium from high concentration locations to low concentration locations in the active material. Diffusion shrinks these concentration gradients over time encouraging uniform concentration throughout an active material particle. However, when a current is applied, transport between the active material and the electrolyte also occurs and concentration changes at the particle surface encourage non-uniformity. As solid-state diffusion is not often infinitely fast compared to the surface flux, this can lead to significantly low or high concentrations at the active material particle surface compared to the interior. The potential of an electrode particle is dependent upon the concentration of lithium at its surface, and therefore poor diffusion can lead to undesirably high or low potentials during charge or discharge, respectively. This change in potential from an ideal case where solid-state transport is infinitely fast is often regarded as an overpotential. This overpotential, as well as overpotential from resistance, is a source of lost energy. Diffusion overpotential stores energy in the concentration gradient of the active material which is later expelled as heat when diffusion occurs, whereas resistance overpotential is just simply expelled as heat immediately. Additionally, these overpotentials may cause the cell voltage limit to be reached prematurely, effectively limiting the capacity of an active material. It is essential that cell voltage limits are not surpassed as potentials that are too high or low can cause

degradation at the surface of the active material even though the interior is at a more stable potential.

3.1 Impact of Geometry on Diffusion Transport

Particle shape is important to consider when measuring impedance from diffusion. A change in concentration is first created at the surface and this encourages changes in concentration further within the active material as time goes on. Figure 3 shows common geometries for modeling diffusion.

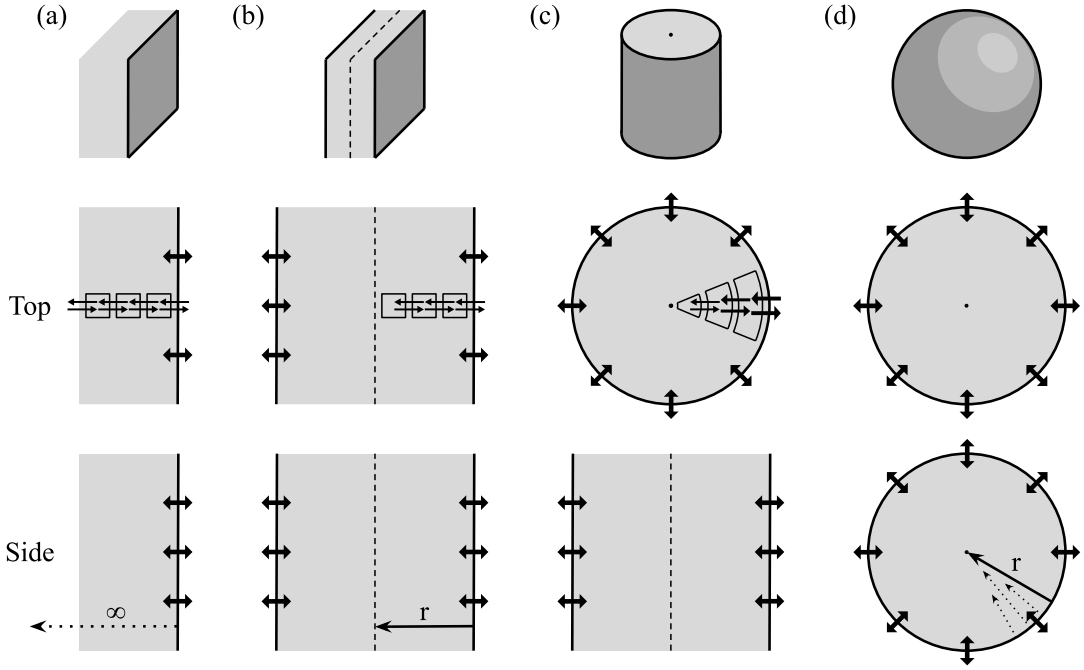

Figure 3: Simplified geometries for modeling diffusion. The given geometries are (a) semi-infinite plane, (b) planar sheet, (c) cylinder, and (d) sphere.

The simplest model is the semi-infinite plane (Figure 3a), a volume that is infinite in all directions except the surface in contact with electrolyte. This is the easiest geometry to model, but in practice, diffusion cannot continue infinitely. Ions transported from the electrolyte will eventually arrive at a position furthest into the interior of the active material

and transport cannot occur further beyond this position. The distance from the electrolyte contacting surface to the furthest interior position is the diffusion length or radius (cm), r, for circular geometries. The planar sheet (Figure 3b) is similar to the semi-infinite plane but instead has two electrolyte contacting surfaces and a central plane forming the furthest interior position. The planar sheet can also be used to model a volume with one electrolyte contacting surface and one non-contacting surface by splitting the geometry in half along the central plane. When ions eventually stop at the end of r, this slows diffusion transport along the diffusion path which causes a greater change in concentration at the electrolyte contacting surface compared to a semi-infinite plane.

The shape of the active material may cause ions to transport inwards from a larger volume to a smaller volume or vice versa. This is the case for the cylindrical and spherical models (Figure 3c-d) which have some radial rather than linear geometry. This will also similarly slow diffusion transport and cause a greater change in concentration at the surface than in a planar sheet or an ideal semi-infinite plane.[1]

In practice, all active materials have finite volumes. While only the sphere is truly finite, all geometries can be used to approximate more complex finite geometries. The planar sheet and sphere mark the maximum and minimum bounds for the volume to surface area ratio (cm), $\tilde{V}/S$, of all geometries with a fixed r. As a result, the planar sheet and sphere also mark the maximum and minimum bounds of diffusion hindrance for geometries with a fixed r.

3.2 Surface Concentration due to Diffusion Transport

The interplay between transport at the active material surface induced by an applied current and transport within the active material determines the concentration (mol cm^{-3}), c, throughout the material. Using Fick's laws of diffusion, the numerical solution to the change in concentration, Δc, of a "relaxed" (starting from a uniform concentration) finite-volume geometry experiencing a constant flux or constant current (CC) pulse has been proven to be[1]

$$X(\tau, y) = \tau + \frac{1}{AQ}\left(\frac{1}{B} + \frac{y^2}{2} - \frac{1}{2} - 2\sum_{i=1}^{\infty} \frac{e^{-\alpha_i^2 Q\tau}}{\alpha_i^2} C(\alpha_i, y)\right), \quad (1)$$

where the ascending, non-zero series α_i and function $C(\alpha_i, y)$ are defined for each geometry as

Planar Sheet: $\sin(\alpha) = 0\ \{\alpha_1 = \pi, \alpha_2 = 2\pi, \dots\}$,

$$C(\alpha, y) = \frac{\cos(\alpha y)}{\cos(\alpha)},$$

Cylinder: $J_1(\alpha) = 0$,

$$C(\alpha, y) = \frac{J_0(\alpha y)}{J_0(\alpha)},$$

Sphere: $\alpha\cot(\alpha) - 1 = 0$,

$$C(\alpha, y) = \frac{\sin(\alpha y)}{y\sin(\alpha)},$$

$X = \Delta c/\Delta c_{tot}$ is the relative change in concentration, $\tau = \Delta q/\Delta q_{tot}$ is the relative change in capacity, $Q = \Delta q_{tot} I^{-1} D_c r^{-2}$ is the relative diffusivity, a normalized measure of how fast diffusion transport is compared to the surface flux, A and B are geometric constants (1 and 3 for a planar sheet, 2 and 4 for a cylinder, 3 and 5 for a sphere, respectively), y is the relative position along the diffusion path on a scale from 0, the center, to 1, the surface,

and J_0 and J_1 are the Bessel functions of the first kind of order 0 and 1, respectively. $\Delta c_{tot} = n_{tot}/\tilde{V}$ is the change in concentration if an arbitrary, desired number of moles (mol), n_{tot}, of ions are transported and uniformly dispersed in a volume (cm^3), $\tilde{V}$, of an active material. $\Delta q = zFn = I\Delta t$ is the capacity (C) acquired after n moles of ions are transported within a certain pulse time (s), Δt, at a current (A), I. z is the ion charge number (+1 for lithium), F is Faraday's Constant ($C\ mol^{-1}$), $\Delta q_{tot} = zFn_{tot}$ is the arbitrary capacity (C) associated with n_{tot}, and D_c is chemical diffusivity ($cm^2\ s^{-1}$), the material property of interest when determining the speed of ion diffusion. τ can also be treated as relative moles transported or relative pulse time given that Δq is proportional to n and Δt when I is constant. I is known to be constant because the ionic flux ($mol\ s^{-1}\ cm^{-2}$), $J = z^{-1}F^{-1}IS^{-1}$, is defined as constant where S is the surface area (cm^2) exposed to electrolyte. This dimensionless convention and equation for describing X resulting from diffusion transport was developed by Atlung, the namesake of AMID and AMIDR. One of the advantages of using dimensionless convention is that it normalizes the variables and describes pulses of all I and active materials of all D_c and r simultaneously as long as the active material geometry is the same.

Figure 4 shows X versus position for a variety of geometries experiencing a positive constant flux pulse starting from a uniform concentration. It can be seen that X first grows near the surface of the geometries where the ions are entering and then disperses throughout the material towards the furthest interior position at the center as τ increases. The difference

between Figure 4a ($Q = 0.5$) and Figure 4b ($Q = 2$) shows that larger values of Q shrink the concentration gradient and better approach uniform concentration during a pulse.

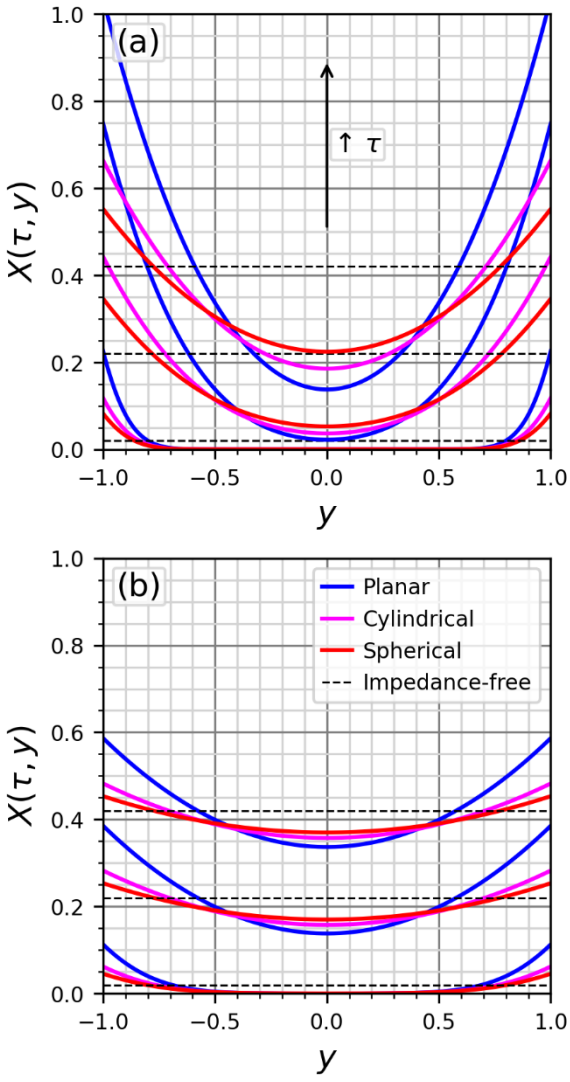

Figure 4: The relationships between relative position, y, relative change in capacity, τ, and relative change in concentration, X, of planar, cylindrical, and spherical active material during a short pulse when relative diffusivity, (a) $Q = 0.5$ and (b) $Q = 2$. These relationships are compared to the ideal, impedance-free relationship when $Q \to \infty^+$.

This equation can be simplified to determine the change in surface concentration, Δc_s, in terms of relative surface concentration, $X_s = \Delta c_s / \Delta c_{tot}$, by setting $y = 1$ returning

$$X_s(\tau) = \tau + \frac{1}{AQ}\left(\frac{1}{B} - 2\sum_{i=1}^{\infty}\frac{e^{-\alpha_i^2 Q\tau}}{\alpha_i^2}\right), \tag{2}$$

where the ascending, non-zero series α_i is defined for each geometry as

Planar Sheet:	$\sin(\alpha) = 0\ \{\alpha_1 = \pi, \alpha_2 = 2\pi, \dots\},$
Cylinder:	$J_1(\alpha) = 0,$
Sphere:	$\alpha\cot(\alpha) - 1 = 0.$

It's unfortunate that the solution to equation 2 must be numerical rather than analytical, but it is at least far simpler than more opaque numerical solutions from techniques such as the Finite Element Method (FEM).

Despite being numerical, equation 2 will often approximate analytical solutions. $\lim_{Q\to\infty^+} X_s(\tau) = \tau$, showing that if D_c is infinitely fast, c in the active material is uniform and c_s has a linear relationship with Δq. This scenario is ideal as this means that no energy will be lost, and the active material can be considered impedance-free. While not obvious, it has been shown that

$$\lim_{\tau\to 0^+} X_s(\tau) = \frac{2\sqrt{\tau}}{A\sqrt{\pi Q}}, \tag{3}$$

Conveniently, all real morphologies will approximate a semi-infinite plane at the start of a CC pulse applied to a "relaxed" active material. This is because the start of a pulse only meaningfully changes concentrations within a very thin layer near the surface which can easily be approximated as a semi-infinite plane.[9] In addition,

$$\lim_{\tau\to\infty^+} X_s(\tau) = \tau + \frac{1}{ABQ}. \tag{4}$$

This shows that as Δq approaches Δq_{tot}, the active material eventually reaches a steady state where X_s approaches a linear relationship with τ, and c_s approaches a linear relationship with Δq. Once this steady state is reached, the pulse can be described as a "complete" pulse that has reached its "end". Using this terminology, a pulse that has been stopped before a steady state has been reached is said to have been stopped before it has reached its end.

Figure 5 shows that the simple analytical equations 3 and 4 form the lower and upper bounds for the otherwise more complex numerical equation 2. While the sphere has the most diffusion limitation from shrinking volumes along the diffusion path and most quickly deviates from equation 3, it is the ideal geometry for minimizing X_s deviation from the impedance-free scenario due to its decreased $\tilde{V}/S$. The difference between Figure 5a ($Q = 0.5$) and Figure 5b ($Q = 2$) shows that larger Q is more desirable to limit X_s deviation from the impedance-free scenario. Lastly, Figures 5a and b have the same shape, but different size. These two graphs could be describing the same pulses, just with a different n_{tot} desired moles of ions to be transported.

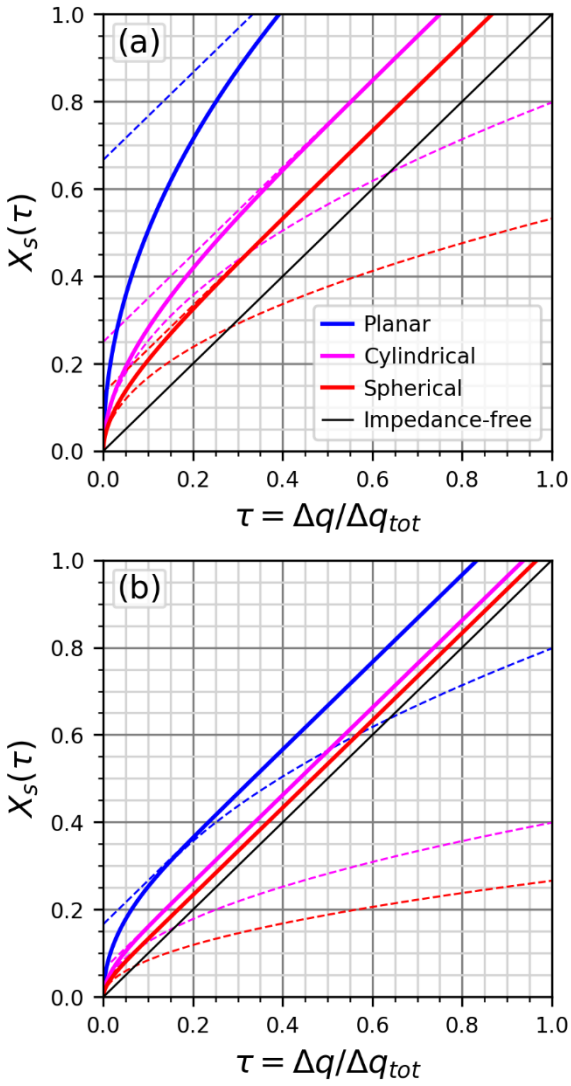

Figure 5: The relationships between relative change in capacity, τ, and relative change in surface concentration, X_s, of planar, cylindrical, and spherical active material during a short pulse when relative diffusivity, (a) $Q = 0.5$ and (b) $Q = 2$. These relationships are compared to the ideal, impedance-free relationship when $Q \to \infty^+$. The inverse quadratic and linear dashed lines, where visible, represent the lower and upper limits for X_s as τ approaches 0 and ∞^+.

3.3 Capacity Limitation due to Diffusion Transport

Poor diffusion can cause the Δc_s to reach a certain limit defined by a voltage limit stopping a pulse before significant utilization of the interior of the active material. This is because the potential of the active material is determined by c_s. This limit can be defined

as when $\Delta c_s = \Delta c_{tot}$ and in dimensionless convention, defined as when $X_s(\tau) = 1$. Inserting this into equation 2 gives

$$1 = \tau + \frac{1}{AQ}\left(\frac{1}{B} - 2\sum_{i=1}^{\infty}\frac{e^{-\alpha_i^2 Q\tau}}{\alpha_i^2}\right), \tag{5}$$

which gives a relationship between Q and τ for when this limit is reached. In the same manner as equations 3 and 4, this relationship can be given the bounds

$$1 = \frac{2\sqrt{\tau}}{A\sqrt{\pi Q}}, \text{ and} \tag{6}$$

$$1 = \tau + \frac{1}{ABQ}. \tag{7}$$

Figure 6 shows this relationship and its bounds. When Q is significantly small, the relationship approaches equation 6 for when τ is small and the limit is reached near the start of the pulse when the internal concentration gradient is still being developed. This is undesirable as a small τ means far less than the desired n_{tot} moles of ions were transported. Alternatively, when Q is significantly large, the relationship approaches equation 7 for when τ is large and the limit is reached near the end of the pulse when the active material has reached a steady state. In this case, nearly all the desired n_{tot} moles of ions are transported.

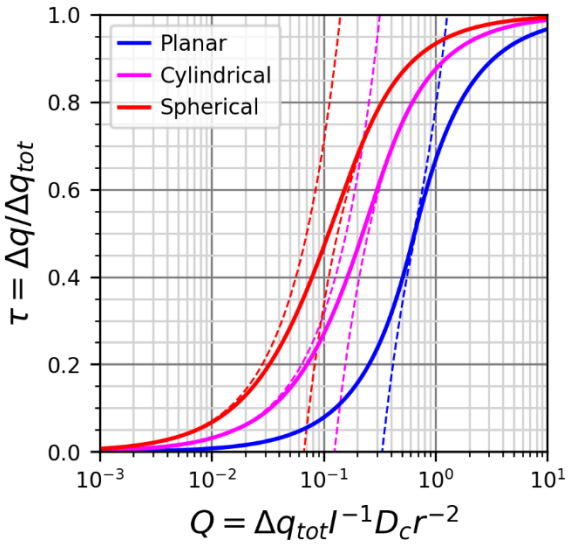

Figure 6: The relationship between relative diffusivity, Q, and relative change in capacity, τ, of planar sheet, cylindrical, and spherical active materials when a relative surface concentration limit is reached, $X_s = 1$, and a pulse is stopped. The exponential dashed lines represent the upper and lower limits for τ as τ approaches 0 and ∞^+.

3.4 Impedance due to Diffusion Transport

In an ideal, impedance-free scenario, the concentration throughout the active material is uniform and the ideal X_s, $X_{s,ideal}$, increases from 0 to 1 equivalently with τ as shown in Figure 5 ($X_{s,ideal} = \tau$). The difference between X_s and $X_{s,ideal}$ can be defined as $X_{s,loss} = X_s - X_{s,ideal}$. $X_{s,loss}$ can also be calculated by simply subtracting τ from equation 2 to get

$$X_{s,loss}(\tau) = \frac{1}{AQ}\left(\frac{1}{B} - 2\sum_{i=1}^{\infty}\frac{e^{-\alpha_i^2 Q\tau}}{\alpha_i^2}\right). \tag{8}$$

Next, this can be converted out of dimension-less convention to get

$$\Delta c_{s,loss}(\Delta t) = \frac{Ir^2}{AzF\tilde{V}D_c}\left(\frac{1}{B} - 2\sum_{i=1}^{\infty}\frac{e^{-\alpha_i^2\frac{\Delta t D_c}{r^2}}}{\alpha_i^2}\right). \tag{9}$$

where $\Delta c_{s,loss}$ is the non-relative difference in surface concentration from an ideal impedance-free scenario. The c_s of an active material determines its potential (V), E, so $\Delta c_{s,loss}$ implies a difference in E from an ideal, impedance free scenario. The relationship between c_s and E for any active material is complex but can be simplified to a simple linear relationship (V cm^3 mol^{-1}), dE/dc, if the E range is small enough. Accordingly, $c_{s,loss}$ can be converted into a diffusion overpotential (V), η_D, for a working electrode as

$$\eta_D(\Delta t) = -\frac{dE}{dc}\frac{Ir^2}{AzF\tilde{V}D_c}\left(\frac{1}{B} - 2\sum_{i=1}^{\infty}\frac{e^{-\alpha_i^2\frac{\Delta t D_c}{r^2}}}{\alpha_i^2}\right). \quad (10)$$

where positive I is now treated as current driving positive ions to leave the active material, the typical convention for working electrodes. dE/dc is not a commonly used metric in cell analysis but differential capacity (C/V), dq/dV is. $q = zF\tilde{V}(c_{sat} - c)$ is the capacity of charge stored in the active material of the working electrode where c_{sat} is the fully saturated concentration corresponding to no charge being stored. $V = E_w - E_c$ is the total voltage (V) of a cell where E_w is the potential of the working electrode and E_c is the potential of the counter electrode. This study uses a half cell arrangement where the counter electrode is lithium metal and will treat $E_c = 0\ V\ vs.\ Li^+/Li^0$. Therefore $dq/dV = -zF\tilde{V}dc/dE$. With this, equation 10 can be further simplified to

$$\eta_D(\Delta t) = \frac{Ir^2}{AD_c\frac{dq}{dV}}\left(\frac{1}{B} - 2\sum_{i=1}^{\infty}\frac{e^{-\alpha_i^2\frac{\Delta t D_c}{r^2}}}{\alpha_i^2}\right). \quad (11)$$

The relationship between Δt and η_D retains the same shape as the relationship between τ and X_s shown in Figure 5. Conveniently, related to equation 4, after a long period of time, equation 11 can be simplified to

$$\lim_{\Delta t \to \infty^+} \eta_D(\Delta t) = \frac{Ir^2}{ABD_c \frac{dq}{dV}}. \tag{12}$$

Even more conveniently, this can be further simplified as

$$R_{D,term} = \frac{r^2}{ABD_c \frac{dq}{dV}}, \tag{13}$$

where $R_{D,term}$ is the terminal diffusive resistance (Ω) given that $V = IR$. This is particularly powerful as this means that the impedance related to diffusion can be approximated as a simple resistance given a long enough period of time. This has a very practical application as it can be used to predict voltage polarization for long, CC charges/discharges or the maximum voltage polarization for intermittent pulses.

3.5 Combining Diffusion Impedance and Resistance

Diffusion is not the only source of impedance in a cell. Impedance can come from a variety of sources from electrical resistance in the current collectors and the conductive additive to ionic impedance in the electrolyte, both in and outside of the electrode pores, and reaction impedance at the electrode-electrolyte interfaces. In addition, many of these impedance sources are paired with capacitances such as double layer capacitance at the electrode-electrolyte interfaces, and parallel plate capacitance across the two electrodes within coin cells. The impedance of the opposing electrode can be ignored if using a

reference electrode and the electrolyte impedance inside electrode pores can be mitigated by using thin electrode coatings. Thin electrodes amplify active material impedances by reducing the total amount of active material, similar to how thin wires produce more resistance. These impedances are diffusion impedance, which is dynamic on long timescales (> 1 s), and interface resistance, R_i, which is effectively instantaneous on long timescales. Remaining sources of impedance are mostly negligible resistances, R_{ohm}, electrical contact resistance and ionic electrolyte resistance, which are also effectively instantaneous on long timescales. Also included is ionic electrolyte diffusion impedance which can be dynamic over long timescales with significantly thick separators, but is effectively instantaneous with standard, commercial thin separators.[10] Therefore, these can simply be treated as a single resistance, $R = R_i + R_{ohm}$, producing a resistive overpotential, $\eta_R = IR$.

In practice, η_R can limit Δq further than η_D alone by allowing a voltage limit to be reached earlier than when $X_s(\tau) = 1$. In this case, the limit can be said to be reached when relative change in voltage, $Y(\tau) = 1$. $Y(\tau) = (\Delta V_i(\Delta t) + \eta_D(\Delta t) + \eta_R)/\Delta V_{tot}$, where $\Delta V_i(\Delta t) = \Delta q(dq/dV)^{-1}$ is the ideal, impedance-free change in voltage after a certain period of pulse time, and $\Delta V_{tot} = \Delta q_{tot}(dq/dV)^{-1}$ is the total change in voltage from the initial voltage to the voltage limit. Evaluating this equation returns

$$Y(\tau) = \tau + \frac{1}{AQ}\left(\frac{1}{B} - 2\sum_{i=1}^{\infty}\frac{e^{-\alpha_i^2 Q\tau}}{\alpha_i^2}\right) + \frac{IR(dq/dV)}{\Delta q_{tot}}. \quad (14)$$

This equation is very similar to equation 2 except for the inclusion of a new term at the end. This new term can be converted into dimensionless units as

$$Y(\tau) = \tau + \frac{1}{AQ}\left(\frac{1}{B} - 2\sum_{i=1}^{\infty}\frac{e^{-\alpha_i^2 Q\tau}}{\alpha_i^2}\right) + \frac{P}{Q}, \tag{15}$$

where $P = RD_c r^{-2}(dq/dV)$ is the relative resistance, a variable comparing η_R to η_D, similar to a Biot number. When $P \ll 1/AB$, Δq is primarily limited by η_D, and the last term can be neglected to simplify the entire equation back to equation 2. However, when $P \gg 1/AB$, the last term is large, and Δq is primarily limited by η_R rather than η_D. Setting $Y(\tau) = 1$ gives the relationship between Q and τ for when a voltage limit is reached,

$$1 = \tau + \frac{1}{AQ}\left(\frac{1}{B} - 2\sum_{i=1}^{\infty}\frac{e^{-\alpha_i^2 Q\tau}}{\alpha_i^2}\right) + \frac{P}{Q}, \tag{16}$$

similar to equation 5 except with the addition of the last term.

Figure 7a shows the relationship posed by equation 15 and Figure 7b shows the relationship posed by equation 16. Increasing P increases η_R and reduces the proportion of τ capable of being transported before a voltage limit is reached. Additionally, Figure 7b shows that increasing P changes the relationship between Q and τ from a pseudo-logistic shape to a pseudo-exponential shape. While the shape of the curve changes significantly with small τ, the shape of the curve remains the same at large τ. This is because η_D approximates η_R when τ is large and the difference between η_D and η_R become indistinguishable without information from earlier in the pulse.

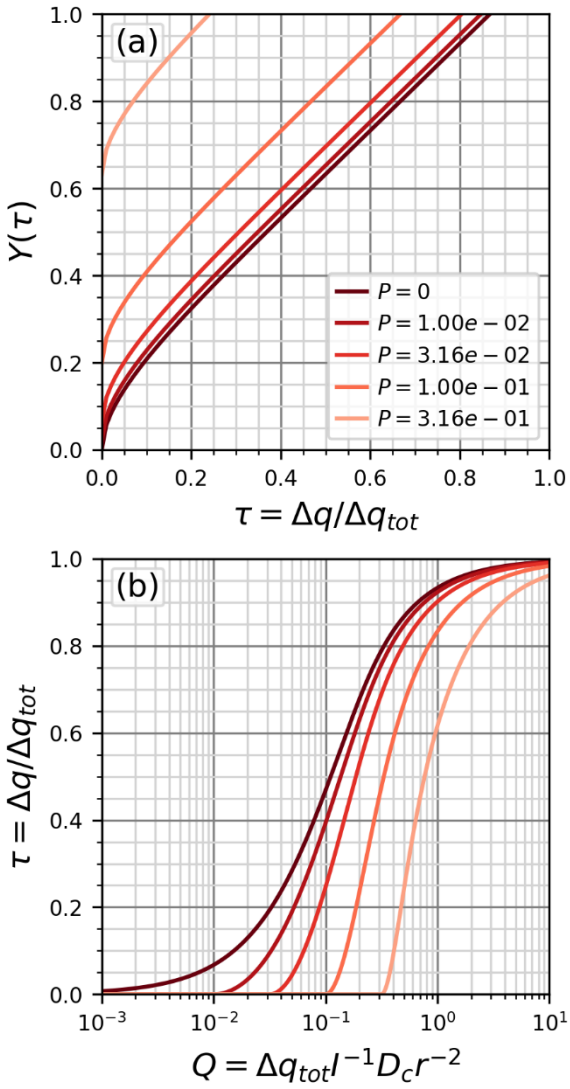

Figure 7: The relationship (a) between relative change in capacity, τ, and relative change in voltage, Y, of a cell during a short pulse when relative diffusivity, $Q = 1$ and the relationship (b) between τ and Q, when a voltage limit is reached, $Y = 1$. The active material is given a spherical geometry and relative resistance, P, is varied to show the impact of resistance.

3.6 Impact of Diffusion Length Variation due to a Particle Size Distribution

The mathematical model for impedance resulting from diffusion is designed for a single geometry but can easily be scaled up for an ensemble of geometries of identical r keeping in mind that I, q, n, and $\tilde{V}$ should represent the total values for the entire ensemble.

However, in practice, geometries such as active material particles often have a measurable variation in r. This presents a problem because ensembles of geometries with varying r do not experience constant flux throughout a pulse which is essential for this model. While flux is equal for all geometries at the start of a pulse, flux at the end of the pulse is proportional to the $\tilde{V}/S$ of a geometry because the I of each geometry is proportional to its q and therefore $\tilde{V}$. This means larger particles increase in flux and smaller geometries decrease in flux throughout the pulse. Despite not being able to develop a complete, simple mathematical model for the impedance of a pulse upon active material with a distribution in r, the bounds for pulses that stop near their start and end with active material of varying r can be calculated. These bounds are simply the original equations 6 and 7 with different average r values, $\bar{r}$, as inputs. These $\bar{r}$ are calculated as $\bar{r}_s = \sum r_j^3 / \sum r_j^2$ and $\bar{r}_e = \left(\sum r_j^5 / \sum r_j^3\right)^{1/2}$ for the start and end of a pulse respectively, where r_j is r for an individual geometry (see Proofs A1 and A2). Figure 8 shows the impact of a theoretical bimodal active material on the relationship between Q and τ. The theoretical bimodal active material used in this model is composed of spheres of r equal to 1 arb. units and 3 arb. units in a 1:1 q ratio. The r used to calculate Q for this bimodal active material is calculated as the capacity-weighted geometric mean as $\bar{r} = 10^{\frac{\sum \log r_j * r_j^3}{\sum r_j^3}}$. The multiplicative change in Q between the uniform and bimodal model can be regarded as a Q-shift calculated as $(\bar{r}_s/\bar{r})^2$ or $(\bar{r}_e/\bar{r})^2$. While the complete model for bimodal active material cannot be plotted, it is clear that it would not differ from a uniform r active material by a dramatic amount. All active materials analyzed in this study have less particle size variation than this theoretical

model, so while particle size variation may add some error to the model, the model is still reasonably accurate (see Table 1).

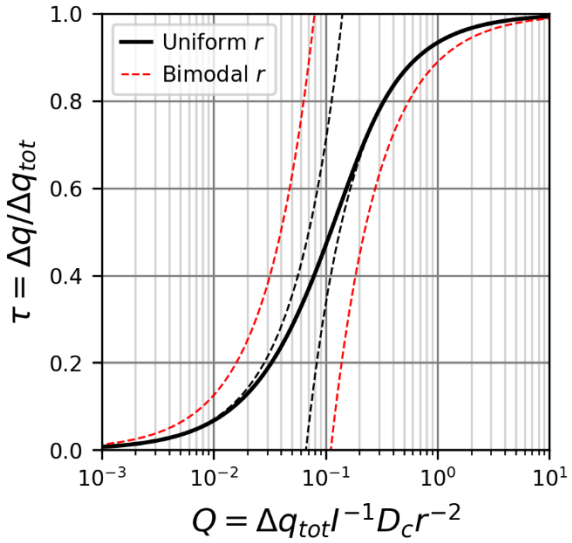

Figure 8: The relationship between relative diffusivity, Q, and relative change in capacity, τ, for uniform and bimodal spherical active materials when a surface concentration limit is reached, $X_s = 1$, and a pulse is stopped. The bimodal active material is composed of spheres of radius 1 arb. units and 3 arb. units in a 1:1 capacity ratio. The diffusion length, r, for the bimodal active material is calculated as the capacity-weighted geometric mean. The dashed lines represent the upper and lower limits for τ as τ approaches 0 and ∞^+.

3.7 Interface Contact Resistivity

While not all resistance in a cell is sourced from the electrode-electrolyte interface, an overwhelming portion can be, especially in cells designed with little active material mass loading. If it is believed that the overwhelming majority of measured R is R_i, then that R_i can be normalized as contact resistivity (Ω cm^2), $\rho_c = R_i S$. This describes the resistivity of current traveling through a film of unknown or infinitesimally thin thickness and is separate from bulk resistivity (Ω cm), which describes the resistivity of current traveling through a bulk material, and sheet resistance (Ω), which describes the resistivity

of current traveling along a film of unknown thickness.[11] In the context of active material, ρ_c is calculated as

$$\rho_c = SR = \frac{ARm}{r\rho_d}, \tag{17}$$

where m is the mass (g) of the active material and ρ_d is the density (g cm^3) of the active material.

3.8 Chemical Diffusivity vs. Tracer Diffusivity

While it is common in literature to report lithium diffusion in Li-ion cells as simply "Li diffusivity" there is more than one kind of D measurement and differentiating between them can be valuable for understanding the mechanisms of diffusion. If an isotope of a solute is used as a tracer to track random particle movement in a uniform concentration, tracer diffusivity, D_t is measured. This is different from chemical diffusivity, D_c, which is measured by observing the transport of a solute from a high concentration to a low concentration. These two are the same in dilute concentrations where all solutes have the same atomic environment and diffusion from a high to a low concentration is driven solely by solute particles independently moving at random. However, in concentrated solutions, D_t stays the same, but D_c changes due to solute-solute interactions not present in dilute concentrations. These solute-solute interactions cause solutes to have the different enthalpies at different concentrations and this difference in enthalpy can drive or hinder diffusion from high to low concentrations.

The relation between chemical potential (J mol^{-1}), μ, and c is known to be

$$\mu(c) = \mu_0 + N_A k_B T ln(\gamma(c)c), \tag{18}$$

where μ_0 is the intrinsic chemical potential (J mol^{-1}), N_A is the Avogadro constant (mol^{-1}), k_B is the Boltzmann constant (J K^{-1}), T is temperature (K), and γ is the activity coefficient. In dilute solutions, γ is constant. In concentrated solutions, solute-solute interactions occur, γ is not constant and the relationship between μ and c is complex. Active materials often have a complex relationship between μ and c because ions are typically stored in solids as concentrated solutions. This is easily observed in q-V plots of active materials which typically do not show a logarithmic relationship. The solute-solute interactions in active materials often present themselves as changes in occupation site enthalpies due to structural distortions at different c.[5] The relationship between D_t and D_c is described by Darken's second equation for a single phase medium,

$$D_c(c) = D_t(c)\left(1 + \frac{dln(\gamma(c))}{dln(c)}\right), \tag{19}$$

where $D_t = D_c$ when γ is constant at dilute concentrations.[12] This can be converted into an equation with more practical variables. Taking the derivative of equation 18 in terms of c gives

$$\frac{d\mu}{dc} = \frac{N_A k_B T}{c}\left(1 + \frac{dln(\gamma(c))}{dln(c)}\right), \tag{20}$$

which share the conversion term given in Darken's second equation. Given this, equation 19 can be simplified to

$$D_c(c) = D_t(c)\frac{c}{k_B T}\frac{d\mu}{dc}, \tag{21}$$

and given that $d\mu = -zFdV$, $zFV_m c = (q_{sat} - q)$, and $F = q_e N_A$, where q_{sat} is the theoretical capacity capable of being stored given complete saturation and desaturation and q_e is the elementary charge (C), it can be made to use dq/dV as

$$D_c(q) = D_t(q)\frac{zq_e(q_{sat} - q)}{k_B T\frac{dq}{dV}}. \tag{22}$$

While D_c is the relevant diffusivity measurement for describing ion transport in the active material of a cell under operation, D_t has a relatively simple derivation modeled by a random walk,

$$D_t = \frac{a^2\left(1 - \frac{c}{c_{sat}}\right)\nu}{2C}e^{-\frac{\Delta G_A}{k_B T}}, \tag{23}$$

where a is the distance between two occupation sites (cm), c_{sat} is the concentration of a completely saturated active material (mol cm^{-3}), ν is the vibrational frequency (s^{-1}), C is the dimensionality constant (2 for a layered oxide where ions are able to transport in 2 dimensions), and ΔG_A is the activation energy (J) of an occupation site hop.[12] The $1 - c/c_{sat}$ term is included to account for the chance that an occupation site hop is blocked by the destination occupation site being already occupied. This term is equivalent to q/q_{sat}. It can be valuable to remove this term to form a new measurement of diffusivity, D_t^*, free-path tracer diffusivity,

$$D_t^* = \frac{a^2 \nu}{2C} e^{-\frac{\Delta G_A}{k_B T}}, \tag{24}$$

which describes diffusion transport for a solute with a uniform c and no occupation sites blocked along its path of travel. This measurement is rather abstract but can be calculated and has powerful implications. The only value in its derivation that is expected to change significantly for an active material at different states of charge is ΔG_A. In this manner, D_t^* can be used as a proxy to measure changes in ΔG_A at different states of charge. If D_t^* stays relatively the same at varying states of charge this suggest that ΔG_A is unchanged, but if D_t^* shrinks significantly, this suggests that ΔG_A has increased significantly. The relationship between D_c and D_t^* is

$$D_c(q) = D_t^*(q) \frac{z q_e q \left(1 - \frac{q}{q_{sat}}\right)}{k_B T \frac{dq}{dV}}. \tag{25}$$

Lastly $R_{D,term}$ can be calculated in terms of site hopping using equations 13, 22, and 23 returning

$$R_{D,term} = \frac{2 C k_B T e^{\frac{\Delta G_A}{k_B T}} r^2}{A B z q_e q \left(1 - \frac{q}{q_{sat}}\right) a^2 \nu}. \tag{26}$$

Chapter 4: Prior Methods

AMID was developed by Marc Cormier, Eniko Zsoldos, and Nuttaphon Phattharasupakun which laid the groundwork for the development of AMIDR.

4.1 Galvanostatic Intermittent Titration Technique (GITT)

GITT is a common single-rate pulse method for measuring D_c. This method is relatively easy to use because the active material is modeled as a semi-infinite plane allowing for the voltage response analysis to be based on equation 3 which is a relatively simple analytical solution. However, active materials of various morphologies only approximate a semi-infinite plane at the very start of a pulse when transport only occurs at the very surface of the particle, so GITT requires the inequality $\Delta t \ll r^2/D_c$ to be true for the approximation to be accurate. Because this inequality relies on D_c, the value whose accuracy is being tested, this inequality must be passed by a very large margin to not suffer from the inequality circularly proving itself. For instance, it has been shown for spherical particles that if $\Delta t D_c/r^2 \approx 0.3$, the measured D_c value will be underestimated by a factor of 10.[9] Because a user would use the D_c value calculated by GITT to check the inequality, the inequality would be calculated as $\Delta t D_c/r^2 = 0.03$ which an inexperienced user might consider as acceptable.

While this may make it tempting to perform GITT with the shortest pulses possible, this can also be problematic as other sources of impedance and capacitive effects are dynamic and relevant on short timescales. Therefore, accurate GITT measurements must be performed within a certain window of Δt that is not always easy for the user to predict

and is very unlikely to be the same at all states of charge of the cell. Additionally, it is possible that under certain conditions, such as when D_c is particularly high or r is particularly small, this window is shrunk out of existence and there is no available Δt that will produce an accurate result.[9]

4.2 Electrochemical Impedance Spectroscopy (EIS)

EIS is a common alternating current (AC) method for measuring D_c. A sinusoidal change in voltage (potentiostatic EIS) or current (galvanostatic EIS) at various frequencies is applied to a cell and the alternating current or voltage response is analyzed respectively. The response at various frequencies is calculated into real and imaginary impedance values and can be made to fit various circuit models that include some or all of the various sources of impedance and capacitance. The sources of impedance and capacitance that are dynamic on short timescales impact the response at high frequencies and diffusion, which is typically relevant on long timescales, impacts the response at low frequencies. Because all elements are being fit simultaneously, EIS does not have the same trouble measuring D_c as GITT does when D_c and other impedance sources are relevant at similar timescales.

Diffusion is very often modeled with a semi-infinite plane as the typical frequencies used are not low enough for the concentration beyond the particle surface to be altered meaningfully. While it has been shown that with significantly low enough frequencies, the impact of active material geometry on impedance can be measured and accurately modeled, this isn't common as low frequencies take longer periods of time to be measured.[13] In addition, very low frequencies suffer from amplified error that must be carefully managed.

This error may be introduced by trying to measure very low currents for potentiostatic EIS, applying currents for very long periods of time adjusting the SOC for galvanostatic EIS, or cell aging for either.

Acquiring D_c measurements at a high resolution versus SOC can also be challenging. Between each measurement, a pulse and a significantly long rest must first be applied to adjust the SOC and allow the cell to relax. Each EIS measurement may also take a significant amount of time if lower frequency measurements are desired. For instance, a single 1 mHz measurement consisting of 10 periods will take greater than 2 hours. This means that measuring a single cell may take an infeasible amount of time considering the availability of EIS capable instruments. Since multiple EIS measurements already require pulses for transitioning SOC, significant time could be saved by using a method that utilizes these pulses as the source of the measurement data using simpler, non-EIS capable instruments.

4.3 Atlung Method for Intercalant Diffusion (AMID)

AMID is a multi-rate pulse method for measuring D_c developed in this lab. As shown in Figure 9, AMID is done by performing a series of pulses and rests at progressively slower currents all with the same voltage limit. The starting voltage of the first pulse and the voltage limit define the voltage interval of a single D_c measurement. After a single measurement, the process is repeated for a new voltage interval. As the last pulse in an interval has a very small current that produces very little overpotential, the starting voltage of a first pulse is very similar to the voltage limit of the previous interval. The voltage

interval is used to define the Δc_{tot} for X_s and total change in capacity of the interval is used to estimate Δq_{tot} for τ. The change in capacity from the end of each pulse compared to the start of the interval is used to define the cumulative change in capacity, Δq_c, of each pulse. Δq_c is approximated as Δq for τ when $X_s = 1$. Given the selection of spherical geometry, a r value measured with SEM images, and the I value corresponding to each pulse, the data is fit to equation 5 using D_c and Δq_{tot} as fitting parameters with the error in τ being minimized (Δq_{tot} is a fitting parameter because the total change in capacity for the interval will be somewhat less than Δq_{tot}). The D_c value acquired is recorded as representative for that interval.

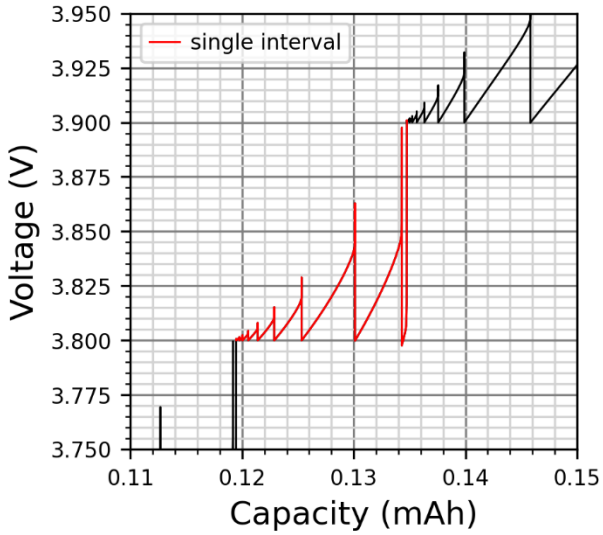

Figure 9: Example of a portion of an AMID protocol in discharge. A single interval composed of descending pulses and ascending rests is highlighted in red.

The approximation of Δq_c as Δq has been shown to be a reasonable approximation for low current pulses that don't result in a small τ.[14] This is because η_D becomes constant and approximates an η_R at the end of a pulse when τ is large. Once η_D has reached a steady

state, it does not matter when the pulse started. η_D will be the same and, therefore, the Δq_c acquired at the voltage limit will be the same as Δq. AMID limits the influence of high I pulses with dynamic η_D by weighting each pulse by the sum of the η_R of all other pulses in an interval. Unfortunately, pulses with dynamic η_D are important for differentiating η_D from η_R. AMID cells are designed to mitigate other sources of impedance through cell build by selecting low impedance electrolyte and low mass loading electrodes to remove electrolyte impedance within the electrode pores and amplify η_D. Unfortunately, reducing electrode mass loading also amplifies R_i by the same proportional amount. This means that AMID will have a systemic error for all active materials with a high R_i. Additionally, the voltage intervals for AMID are typically rather large (0.1 V or greater) limiting the SOC resolution.

Chapter 5: Atlung Method for Intercalant Diffusion and Resistance (AMIDR)

AMIDR is a new method for measuring D_c similar to AMID but with a series of modifications such as the use of a GITT-style, single-rate, iterating pulse and rest protocol shown in Figure 10, and a novel approach for accounting for resistance. Exact details necessary for replication of this study are available in Chapter 6: Experimental, whereas design considerations are given within this section.

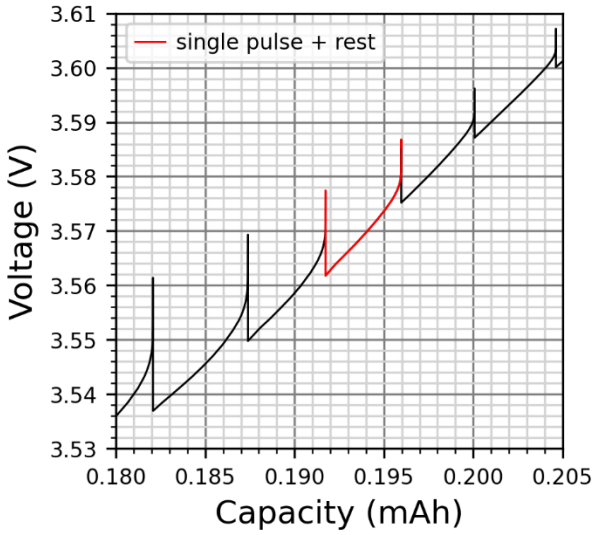

Figure 10: Example of a portion of an AMIDR protocol in discharge. A single descending pulse and ascending rest is highlighted in red.

5.1 Cell Design

AMIDR cells are quite similar to AMID cells in that they have very low mass loading and electrolyte selected to reduce impedance. Mass loading is reduced to the point that the current collector is somewhat visible beneath the electrode coating. This ensures that there are no particles layered on top of each other limiting the electrolyte impedance within the pores to be negligible. In addition, it also reduces the active material mass

amplifying the active material impedance sources, diffusion impedance and interface resistance. These very low mass loading coatings can be achieved by reducing the active material:solvent ratio and selecting a very low-profile coating blade.

Different from AMID, AMIDR cells typically use a reference electrode. The reference electrode allows the counter electrode impedance to be neglected which is valuable as the counter electrode typically has impedance that develops on a similar timescale as the working electrode impedance and, therefore, cannot be neglected as simply R. The reference electrode selected is a 50 μm Au wire insulated with a 7 μm polyimide coating often referred to a micro-reference electrode (μ-RE). After cutting and stripping the polyimide coating on either ends of the wire to allow for electrical contact, the wire is threaded into a coin cell during the cell build process (see Section 6.3 for additional details). Once the cell is built, the reference electrode must be lightly lithiated to produce a AuLi alloy. This alloy has been shown to produce a stable ~0.31 V vs. Li^+/Li^0 which allows it be used as a reference electrode.[4,15]

5.2 Testing Apparatus

The reference electrode has very little contact area with the electrolyte which gives it a significant amount of resistance and very little double layer capacitance at its interface. This means that even a small amount of induced current from ambient electromagnetic radiation will contribute to a very large change in the measured potential. In this manner, the reference electrode can act like an antenna unless properly shielded. The only way to ensure that the reference electrode does not produce any induced current is to shield the

entire cell and all its wires up to the cell tester. This can be done with shielded cables and aluminum foil attached to a ground in combination with an insulating wrapping material such as nitrile gloves to prevent shorts and ground loops (see Figure 14).

AMIDR cannot be performed accurately on just any cell tester. The cell tester must be able to apply and measure a current with reasonable accuracy (± 1 μA), but great stability (± 1 nA) within a period < 0.1 s from the start of the pulse. This is because while AMIDR will work with any current small enough, that current needs to be kept stable and measurable for the assumption of constant flux at the active material surface to be held true. Similarly, the cell tester must be able to measure and record voltage at high frequency (< 0.1 s) and great accuracy (± 0.1 mV). This voltage measurement accuracy requirement can be compensated for with even higher frequency measurements by averaging voltage measurements together to produce voltage measurements with less noise. These requirements have been determined for coin cells with Li layered oxide active material and the requirements might need to be adjusted for different cell formats and active materials. For instance, a very low mass loading pouch cell will likely not require such low current accuracy and an active material with rapidly changing impedance over a small change in voltage will likely require more accurate voltage measurement.

5.3 Data Analysis

Rather than using a multi-rate pulse protocol like AMID, AMIDR uses a single-rate pulse protocol similar to GITT. This allows for a greater resolution of D_c over SOC.

Additionally, while AMIDR is still based upon the mathematics described by Atlung, modification is made to account for R.

While it may be tempting to define ΔV_{tot} as the total change in voltage of the pulse and simply fit Y over τ of a single pulse to equation 15 as shown in Figure 7a, this equation is not well suited for fitting. Firstly, the initial slope of Y over τ is infinite meaning that any slight error in τ due to error in current measurement or cell capacitive effects will result in a massive error in Y which is an issue if the fit is produced by minimizing error in Y. Secondly, τ and Y are much larger towards the end of the pulse which means that minimizing error in τ or Y will give significantly more weighting to the end of the pulse.

Instead, ΔV_{tot} is defined as the change in voltage from the pulse start for each individual data point and the total dataset is then fit to equation 16 as shown in Figure 11a and b. In this manner, $Y(\tau) = 1$ is set for each individual data point as if each data point reached its own voltage limit. For clarity's sake, it is helpful to change a few variable names. $\Delta q_{tot} = (dq/dV)\Delta V_{tot}$ can be rewritten as $\Delta q_i = (dq/dV)\Delta V$ where Δq_i is the ideal, impedance-free change in capacity corresponding to ΔV, the actual change in voltage, of every point. Q and τ are now redefined as $Q = \Delta q_i I^{-1} D_c r^{-2}$ and $\tau = \Delta q/\Delta q_i$. dq/dV is calculated as $dq/dV = \Delta q_0/\Delta V_0$ where Δq_0 and ΔV_0 are the changes in capacity and voltage from the start of the pulse to the termination of the relaxation period after the pulse. In this manner, the calculated dq/dV is free from impedance and purely thermodynamically determined. Given the selection of spherical geometry and Δq as the change in capacity for each point, the pulse is fit to equation 16 using Q and P as fitting

parameters with the error in τ being minimized. Then, given a r value measured with SEM images and I for the pulse's current, R and D_c are calculated. Lastly, ion saturation and D_t^* can optionally be calculated with the assistance of regular mass loading cell data to account for poor active mass accuracy when using low mass loading cells.

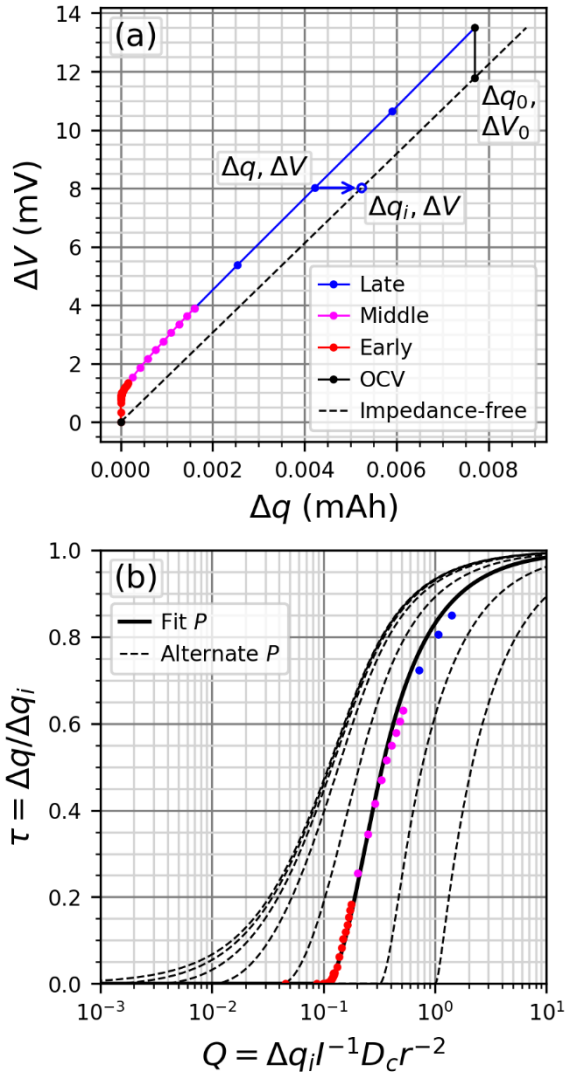

Figure 11: The transformation of pulse data to optimize fitting accuracy from (a) a pulse plotted with widely recognizable axes of change in capacity, Δq, and change in voltage, ΔV, to (b) the same pulse plotted with axes of relative diffusivity, Q, and relative capacity, τ, which is much better suited for fitting because all periods of the pulse are equally weighted.

This method using equation 16 is much better suited for fitting as the greatest change in τ over change in Q is not vertical mitigating any error in τ produced by error in Q. Additionally, because error in τ is being minimized and τ is a normalized measurement of capacity, equal weighting is given throughout the pulse. Lastly, spherical geometry is selected as most active materials have a form that is more spherical than it is cylindrical or planar. Technically, layered oxides might be better represented as a series of cylinders of varying r as diffusion primarily occurs within the layers of the lattices. However, due to the inconsistent flux that these cylinders experience due to varying r, this representation cannot be explained by the simple mathematical model presented in this study. Regardless, there is relatively little difference (less than a factor of 3) between the values of D_c measured by fitting to a cylindrical or spherical model because there is relatively little difference between the values of Q for a cylindrical and spherical model as seen in Figure 6.

All of these steps of analysis as well as data visualization tools are combined into a user friendly, python program designed to allow users with minimal programming experience to run their own AMIDR experiments and rapidly analyse AMIDR test files. This program is built off the AMID framework and therefore can analyze AMID test files as well. In addition, it also includes a series of optional features to help with cell tester file format conversion, fitting of erroneous data, and even the ability to analyse AMID datasets with AMIDR mathematics (even though this is typically not recommended). Also included within the package containing this program are the datasets analyzed within this study, so

that a new user can practice the analysis process, and an experienced impedance expert can verify the results presented here.

5.4 Protocol Design

AMIDR analyzes a series of single-rate discharge pulses followed by a series of single-rate charge pulses after 1.5 cycles of formation (see Figure B1). This protocol is split between multiple protocol instruction files due to cell tester limitations but also to allow for some flexibility during the entire test. Each of these instruction protocol files produces one results file each that get combined within the AMIDR program. AMIDR is designed to perform comparison between charge and discharge results to confirm accuracy. This does not necessarily have to be unique for AMIDR. While many papers simply report discharge results for GITT, a comparison of charge and discharge results could also be an easy way a lot more confidence to GITT results. Single-rate pulses require three parameters to be selected: voltage limit spacing, the pulse current, and the relaxation time between pulses.

Decreasing the voltage limit spacing increases the total number of pulses providing more resolution but also increases test time. There are also hard limits to the voltage limit spacing. The voltage limit spacing must be substantially larger than the instrument's voltage resolution for $Y(\tau) = 1$ to be accurate. Alternatively, the voltage limit spacing must be small enough for the dq/dV of the active material to be consistent throughout the pulse. If two adjacent pulses have a significant difference in dq/dV, then there is likely a large change of dq/dV within each pulse as well. A good rule of thumb is that the dq/dV

of a pulse should not differ from a proceeding or succeeding pulse's dq/dV by a factor of 2 or greater. This means that AMIDR struggles with measuring D_c when dq/dV changes rapidly over a small change in V. On a q-V plot these troublesome areas appear as plateaus which are associated with phase changes. One strategy for dealing with these q-V plateaus may be to set a capacity limit in addition to a voltage limit, but this was not attempted for this study.

Increasing current decreases the total test time, but current must be set low enough that a complete pulse is achieved by the time the pulse's voltage limit is reached. This is roughly defined as when $\tau > 0.5$, but larger τ values are even more accurate. Considering equation 7 which describes the lower limit for τ as a result of Q, the maximum current limit can be estimated as $I < 0.5ABdq/dV\Delta V_{tot}D_c r^{-2}$ where ΔV_{tot} can be estimated as the voltage limit spacing. This means that reducing the voltage limit spacing also reduces the maximum current that can be applied increasing test time further. Additionally, current may need to be reduced further for cells with high resistance as this can also cause the voltage limit to be reached prematurely. While this does mean that some parameters need a broad estimate of D_c before testing begins like GITT, it is unlike GITT in that there is a process independent of D_c to detect if the parameters are inadequate after testing.

Decreasing relaxation time decreases the test time, but relaxation time must be long enough to achieve "complete" relaxation. Complete relaxation, like complete pulses, is not 100% achievable, but can be approached to a satisfactory level. The amount of time it takes for active material to relax to a uniform concentration is comparable to the amount of time

it takes for active material to reach a steady state during a pulse. This is useful because this means that relaxation times that are at least as long as the complete pulses proceeding and succeeding them allow for adequate relaxation. For example, the recommended relaxation time for active material measured with 80 C/80 pulses is > 1 hour as each pulse is expected to last for about 1 hour with some variance due to changing dq/dV. It is recommended to set the relaxation time somewhat longer for active materials with significant change in dq/dV as pulses completed when dq/dV is high will be longer.

It is recommended to first determine the desired voltage limit spacing and then select appropriate current and relaxation times dependent on this voltage limit spacing. These parameters can also be adjusted for different ranges of SOC. For instance, it is recommended to use smaller voltage limit spacing for ranges of SOC where D_c changes rapidly and smaller current and longer relaxation times for ranges of SOC where D_c is small. In this study, a different set of parameters were selected for active materials at low SOC to compensate for the rapid decrease in D_c typical for layered oxides (see Table 2). For novel materials, AMIDR may have to be run multiple times to tune in each measurement over SOC, but the parameters selected for this study should be adequate for layered oxides. Especially small voltage limit spacing and current are recommended specifically for charging pulses at low SOC. This is because the initial poor D_c at low SOC can cause the first few charging pulses to hit their voltage limits rapidly producing incomplete pulses without enough pulse time for the SOC to change substantially. Eventually a pulse with a voltage limit outside the low SOC range occurs producing a rather long pulse that charges the cell until it is well outside of the low SOC range.

Reducing the voltage limit spacing allows for more low SOC pulses to be performed allowing for more capacity to be drawn inside the low SOC range without the voltage limit reaching too far outside. Despite tailored parameter selection for low SOC, the lowest SOC pulses during charge or discharge are generally not complete pulses due to their very poor D_c. If a user can detect that incomplete pulses are being measured during discharge ($\tau > 0.5$), it is recommended to finish that section of the test and start the next charging protocol with a full relaxation step in between. Lastly, changing protocol parameters within the test allows for an additional method of confirmation of results. If results remain continuous when protocol parameters change this informs the user that the protocol parameters are adequate and do not contribute error to the results.

It is desired to evenly weigh the pulse datapoints from the start to the end. Regarding Figure 6, this suggests that a logarithmic distribution of Q values would be optimal for sampling with even weighting throughout. Considering $Q = \Delta q_i I^{-1} D_c r^{-2}$ and $\Delta q_i = (dq/dV)\Delta V$, this suggests that a logarithmic distribution of Δq_i and therefore ΔV would be ideal, but this is not entirely feasible with most cell testers. Most cell testers do not have an option for designing protocols with logarithmic sampling rates and the voltage resolution of the cell tester might not be accurate enough to properly trigger recording of a datapoint, especially when voltage resolution is being compensated for by averaging of high frequency datapoints. Because Δq_i and Δq only vary by a factor of τ and $\Delta q = I\Delta t$, time sampling is an adequate replacement for voltage sampling. Δq_i and Δq can vary significantly on a logarithmic scale when τ is very small, but the error in τ is also very small when τ is small, so the impact of any "oversampled" datapoints will be negligible

and not be consequential to the entire fit. Most cell testers do not have an option for logarithmic time sampling either, but this can be approximated by using a series of steps to approximate a logarithmic distribution. More specifically, a protocol can be designed with a series of seamless CC steps sampling every 0.1 s for 1 s, every 1 s for 9 s, every 10 s for 90 s, and so on. This gives a datapoint distribution similar to the tick distribution on a logarithmic plot and an acceptably equal weighting of datapoints across the entire pulse.

5.5 Error Management

Not all cells will return accurate results and cells can fail before testing even begins. Because coin cells are not designed with Au wire reference electrodes in mind, the reference electrode can often be the source of cell failure. It is recommended to build three times as many cells as intended to analyse due to the relatively high but manageable rate of cell failure. Firstly, the reference wire may be snipped during the cell crimping step due to the pressure required to seal the cell. Secondly, the insulation surrounding the reference wire may be pierced as well leading to shorts between electrodes. These can either be hard shorts coupling the potentials of two electrodes together, or soft shorts which may not be immediately apparent. Occasionally, delithiation of the reference electrode can be observed when the reference electrode potential strays far away from ~0.31 V vs. Li^+/Li^0, and self-discharge of the cell can be observed when the terminations of rest periods for charge and discharge do not align on a q-V plot (see Figure B2). It is likely that these are due to soft shorts within the coin cell and should be checked before further analysis. Checking for sources of error and outliers is formal part of the analysis process in the AMIDR program.

Analysis of quality cells will almost always return some erroneous pulses. There are three ways that erroneous pulses can be detected. Firstly, the pulse data may not be able to fit to the model within the fit parameter bounds. This may be due to a multitude of reasons but most commonly occurs in extreme examples of the other two ways pulses may be detected as erroneous. Secondly, significant changes in dq/dV during a pulse can lead to inaccurate fits as the model expects dq/dV to remain consistent (see Figure B3). This is detected by comparing the dq/dV of pulses with the dq/dV of their adjacent pulses. If there is a difference in dq/dV of a factor of 2 or greater between two adjacent pulses, it is recommended to ignore both pulses. Additionally, it is also recommended to ignore the first and last pulse as their dq/dV cannot be ensured to be steady. Lastly, if a pulse is stopped before diffusive impedance reaches a steady state then that pulse is considered incomplete and should be ignored (see Figure B4). This is recommended to be when the pulse ends with $\tau < 0.5$. This pulse removal process can be done within the AMIDR program and the maximum factor of dq/dV change and the minimum τ can also be adjusted within the AMIDR program. The remaining pulses typically have good fits with low fit error calculated as $\sqrt{\sum(\tau_{exp} - \tau_{mod})^2} / \left(m * \max\left(\tau_{exp}\right)\right)$ where τ_{exp} are the relative capacities of the experimental dataset, τ_{mod} are the relative capacities of the model sharing the same Q values as τ_{exp}, and m is the total number of τ_{exp} datapoints (see Figures B5 and B6).

Chapter 6: Experimental

SEM measurements and analysis were done by the author and Ines Haman, while XRD measurements and analysis were done by Ines Haman, Svena Yu, and Ning Zhang.

6.1 Scanning Electron Microscopy (SEM) Imaging and Particle Sizing

SEM images were taken with a ThermoFisher Scientific AxiaSEM (USA). The materials were placed onto a conductive carbon tape adhered to a stub for SEM imaging. A Secondary Electron detector was used in high-vacuum mode, and the images were collected at an accelerated voltage of 5 kV and a current of 12 pA.

An image containing at least 200 particles such as Figure 12a was selected for each material and the particles were given boundaries by hand with a paintbrush tool. These boundaries are then recognized by a simple image analysis software, ImageJ, and the particles individualized such as in Figure 12b and assigned an area using the scale defined by the SEM. The radii of the particles are then calculated as $r = \sqrt{A/\pi}$ and averaged using the capacity-weighted, geometric mean as $\bar{r} = 10^{\frac{\sum \log r_j * r_j^3}{\sum r_j^3}}$. Additionally, $\bar{r}_s = \sum r_j^3 / \sum r_j^2$ and $\bar{r}_e = \left(\sum r_j^5 / \sum r_j^3\right)^{1/2}$ for calculating the start and end bounds considering diffusion length variation are also calculated to check and ensure that the particle size distribution is not too wide. Table 1 shows that all active materials analyzed by SEM had relatively similar particle sizes and limited size variation.

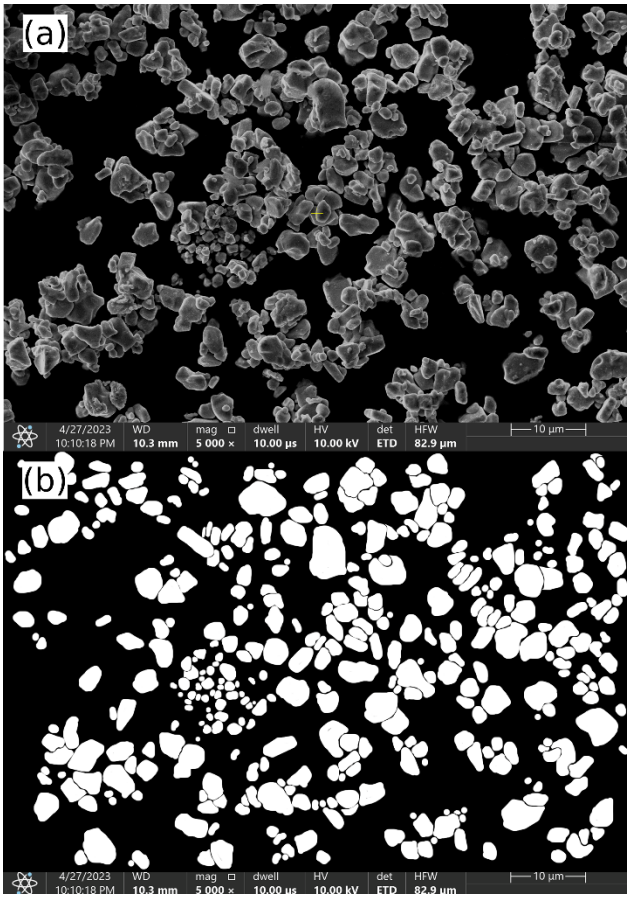

Figure 12: NMC811 example of a scanning electron microscope (SEM) image (a) before and (b) after particle individualization.

Table 1: Results of Particle Size Averaging

Material	$\bar{r}$	$\bar{r}_s$	$\bar{r}_e$	**Pulse Start Q-shift** $(\bar{r}_s/\bar{r})^2$	**Pulse End Q-shift** $(\bar{r}_e/\bar{r})^2$
NMC640	0.784 µm	0.737 µm	0.871 µm	0.884	1.23
NMC811	1.736 µm	1.607 µm	1.947 µm	0.857	1.26
NM9505	1.318 µm	1.173 µm	1.596 µm	0.792	1.47

6.2 Electrode Construction

For low mass loading electrodes, cathode active material (Zhenhua NMC640, Umicore NMC811, Zhenhua NM9505), Super-S carbon black, and polyvinylidene fluoride

(PVDF) were combined in a ratio of 84:8:8 by weight. Then, N-methyl-2-pyrrolidone (NMP) was added as a solvent to form a 33% solids weight slurry after mixing in a planetary mixer (Mazerustar) for 300 s. The slurries were then coated onto Al foil using a 38 μm notch bar upon a smooth glass plate and dried in an oven at 120 °C for 1 hour, resulting in coatings with partially visible Al foil and mass loadings of 0.6 – 2.4 mg cm^{-2} depending on the active material used. Next, the electrode sheets were calendared at a pressure of ~2000 atm and punched into 1.275 cm diameter discs.

6.3 3-Electrode Coin Cell Assembly

The reference electrode, a 50 μm diameter Au wire with a 7 μm thick polyimide insulation (Goodfellow Cambridge Ltd., United Kingdom), was cut into lengths of 2 – 3 cm. Each end was then cut or stripped with a scalpel under an optical microscope at 50X. The exterior end was stripped on one side as shown in Figure 13a for a length of ~4 mm to later ensure contact with solder used to connect to a Ni contact tab. The interior end was cut by getting the scalpel underneath the polyimide coating as if to begin stripping and then rotated downward and cut at a 30 – 60° angle. This ensured a small interface with the electrolyte without risk of the metallic end being sealed off by the polyimide coating which can happen if just the wire is simply cut at a 90° angle. Then the middle of the wire was secured between a 2325-type coin cell casing top cap clipped to a polypropylene gasket. Next, the cap assembly, coin cell casing bottom can, spacer, spring, and positive electrode were dried in a 110 °C vacuum antechamber overnight before being entered into a glovebox. Inside the glovebox, the coin cell was assembled upside down with the cap assembly first as show in Figure 13b. The negative electrode, a lithium metal foil, was

placed in contact with the spacer before being covered by a 20 μm separator (Celgard 2300), the interior reference electrode end, 75 μl of 1.5 M $LiPF_6$ in ethylene carbonate (EC):dimethyl carbonate (DMC) electrolyte (1:1 v/v), and another separator in that order. Lastly, the cathode and can were placed on top, and the cell crimped and sealed with the exterior reference electrode end placed on top of the cap to avoid shearing of the wire. Lastly, after removing from the glovebox, the exterior reference electrode end was soldered into a folded Ni contact tab and covered and protected by dried epoxy (Loctite EA-1C) as shown in Figure 13c.

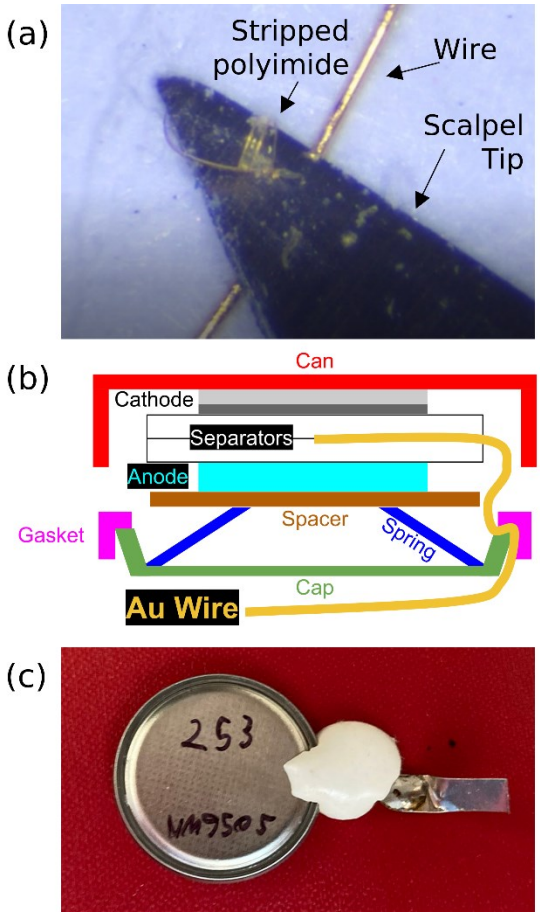

Figure 13: Custom reference electrode coin cells. (a) Stripping of the wire under optical microscope with a scalpel, (b) cross section schematic of the 3-electrode coin cell assembly, (c) appearance of a 3-electrode coin cell after epoxy has set.

6.4 Reference Electrode Lithiation

The reference electrode was lithiated against the cathode at 150 nA for 1 hour by a BioLogic VMP-3e and allowed to relax for > 1 hour until the reference electrode's potential settled at ~0.31 V vs. Li^+/Li^0. Because I was so small the change in the cathode's SOC was negligible.

6.5 Cell and Wire Shielding

Figure 14 shows the steps of the cell shielding arrangement. The BioLogic VMP-3e was selected for AMIDR testing and comes with wires partially shielded by a shielded

cable up to ~10 cm near their ends. These wires were attached to a BioLogic CCH-1 4-point connection coin cell holder where the coin cell was held. First, the coin cell holder and all wires except the ground wire were sealed inside a nitrile glove with the open end tied around the shielded cable and the end of the ground wire with a twist tie. The ground wire was then attached to a sheet of aluminum foil which was wrapped entirely around the nitrile glove and tightly sealed around the shielded cable. Then, the aluminum foil was sealed inside a second nitrile glove with the open end again tied around the shielded cable with a twist tie. Lastly, the cells were tested in a metallic temperature box which provided an extra layer of shielding.

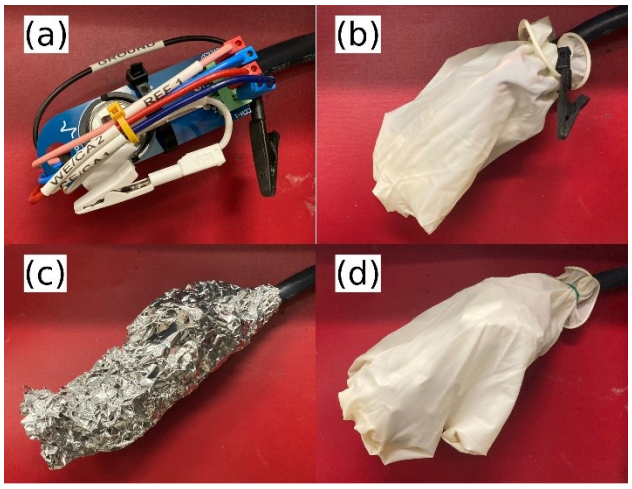

Figure 14: Shielding steps: (a) Uncovered cell holder wrapped into a tight form factor, (b) cell holder wrapped in a first layer of insulating nitrile glove with ground wire out, (c) cell holder wrapped completely with aluminum foil attached to the ground wire, (d) cell holder wrapped in a second layer of insulating nitrile glove.

6.6 AMIDR Protocols

All cells began with a 1.5 cycle formation protocol consisting of a C/20 charge to 4.2 V, a C/20 discharge to 3.0 V, another C/20 charge to 4.2 V, and a 15 minute V hold at 4.2 V. After this, pulse protocols were applied with the parameters given by and in the

order of Table 2. In between protocols are unrecorded rest steps with longer than the prescribed rest times often up to a day or two. The standard protocol was used for NMC640 and NMC811 materials. The beta protocol was used for NM9505 early in development of AMIDR, but otherwise the high resolution protocol was used for NM9505 to get better detail to compensate for its higher variance dq/dV.

Table 2: Pulse Protocol Parameters

Test	Parameters	4.2-3.95 V	3.95-3.7 V	3.7-3.5 V	3.5-3.7 V	3.7-3.95 V	3.95-4.2 V
Standard	V Limit Spacing	25 mV		25 mV	10 mV	25 mV	
	Rate	C/40		C/120	C/300	C/40	
	Rest Time	1 hour		4 hours	4 hours	1 hour	
Beta	V Limit Spacing	25 mV		25 mV	25 mV	25 mV	
	Rate	C/40		C/120	C/120	C/40	
	Rest Time	1 hour		4 hours	4 hours	1 hour	
High Res	V Limit Spacing	12-13 mV	12-13 mV	12-13 mV	10 mV	12-13 mV	12-13 mV
	Rate	C/80	C/80	C/240	C/300	C/80	C/80
	Rest Time	1 hour	1 hour	4 hours	4 hours	1 hour	1 hour

Table 3 gives some GITT protocol parameters found in published work for comparison to AMIDR. While each protocol is different and performed on a different material some generalities can be determined. Firstly, it is unlikely many complete pulses were obtained given the generally short pulse duration times and the high rates used. Secondly, there does not appear to be any rigorous justification for the relaxation times, so they may not be adequate for every measurement. Lastly, given the larger number of pulses taken and lack of tuning of parameters for different SOC, these tests likely took a lot longer than the typical AMIDR test.

Table 3: Common GITT Protocol Parameters[16]

Rate	Pulse Duration Time	Relaxation time
C/10	5 min	2 h
C/20	90 min	5 h
C/10	10 min	40 min
C/10	20 min	2 h
C/20	60 min	4 h
C/5	10 min	40 min
C/20	15 min	45 min
C/10	10 min	2 h
C/10	20 min	1 h
C/10	5 min	1 h
C/10	30 min	2 h
C/20	20 min	2 h
0.4 C	5 min	3 h
C/25	90 min	10 h
C/20	120 min	10 h

The protocols used are available in the package containing the AMIDR program. These protocols can be lightly modified for different materials, but care should be taken to not disturb a few key elements that are essential to allow the AMIDR program to properly read and analyze the results. Each pulse is composed of a series of CC steps sampling every 0.001 s for 1 s, 0.01 s for 9 s, 0.1 s for 90 s, 1 s for 900s, and 10 s indefinitely. Additional steps could be added to a pulse, but it was not expected that a pulse would last longer than 10,000 s. The AMIDR program automatically averages 100 recorded datapoints together so that each step contributes 9 (or 10 for the first step) high voltage resolution datapoints

for analysis. If additional datapoints are recorded, the datapoints would achieve better voltage resolution, but the recorded files would also be larger. Each rest period is composed of a long rest step and two short 0 A CC steps. When a rest step is applied, this means that the galvanometer of the cell tester is physically disconnected, whereas a 0 A CC step means that the galvanometer is connected to the cell, and 0 A of current is aimed for, but a small amount of current is still recorded. The rest step is therefore desired to prevent unexpected change in SOC during long rest periods. However, when the galvanometer is reconnected at the transition from a rest step to a CC step, it introduces a small amount of static charge to the cell which can impact the measured voltage. Therefore, two 0 A CC steps are included. One to allow the static charge to dissipate, and a second to capture a high resolution relaxed cell voltage before a pulse. The AMIDR program automatically recognizes these different steps and analyzes them accordingly. It's important to note that at the start of the beta protocol the issue with reconnection of galvanometer producing static charge was not realized and the results include unaccounted for ΔV at the beginning of the pulses. This error was fixed at ~4.0 V during discharge, but pulses before this had somewhat erroneous D_c and very erroneous R measured.

6.7 AMIDR Analysis Parameters

All cell data was analyzed with the single pulse AMIDR program with default settings. The pulse data analyzed was the measured potential of the active material versus the reference electrode while the results are labeled with the active material potential versus the lithium metal anode. All pulses were fit to the spherical model and used the inputs listed in Table 4 to calculate D_c, Li saturation, and D_t^*. The specific capacities of low mass

loading cells are hard to measure due to small and inaccurate active mass measurements and amplified formation side reactions. Therefore, the recorded specific capacities are linearly adjusted to match the specific capacities of regular mass loading cells at certain voltages. The active material density value used to calculate ρ_d was 4.9 g cm^{-3} for all materials as any error in this value is inconsequential on a logarithmic scale.

Table 4: Fitting and Calculation Parameters

Material	Radius	Temperature	Theoretical Fully Desaturated Capacity	Regular Loading Datapoint 1		Regular Loading Datapoint 2	
NMC640	0.784 μm	303.15 K	279 mAh/g	74 mAh/g	3.8 V	148 mAh/g	4.1 V
NMC811	1.736 μm	303.15 K	275.5 mAh/g	70 mAh/g	3.7 V	178 mAh/g	4.1 V
NM9505	1.318 μm	303.15 K	275 mAh/g	66 mAh/g	3.7 V	149 mAh/g	4.0 V

6.8 X-ray Diffraction (XRD) and Ni in Li Layer (Ni_{Li}) Calculation

Powder XRD spectra were obtained using a Bruker D8 diffractometer with a Cu target X-ray tube and a diffracted beam monochromator. The spectra were collected over a scattering angle range of 15° to 70° in 0.02° steps at 3 s per step. The lattice parameters and cation-mixing rates were determined from refinements made with the Rietveld structure refinement software Rietica using the R-3m space group. Li was assumed to occupy 3a sites (lithium layer) while the 3b sites (metal layer) contained Ni, Mn, and Co and 6c sites contained oxygen. The exchange of Ni and Li between 3a and 3b sites was allowed with the constraint of maintaining the stoichiometry of the material.

Powder XRD was accomplished primarily to determine Ni_{Li} to compare to D_c results. Figure 15 shows the spectra results and Table 5 shows the results of the Reitveld refinement.

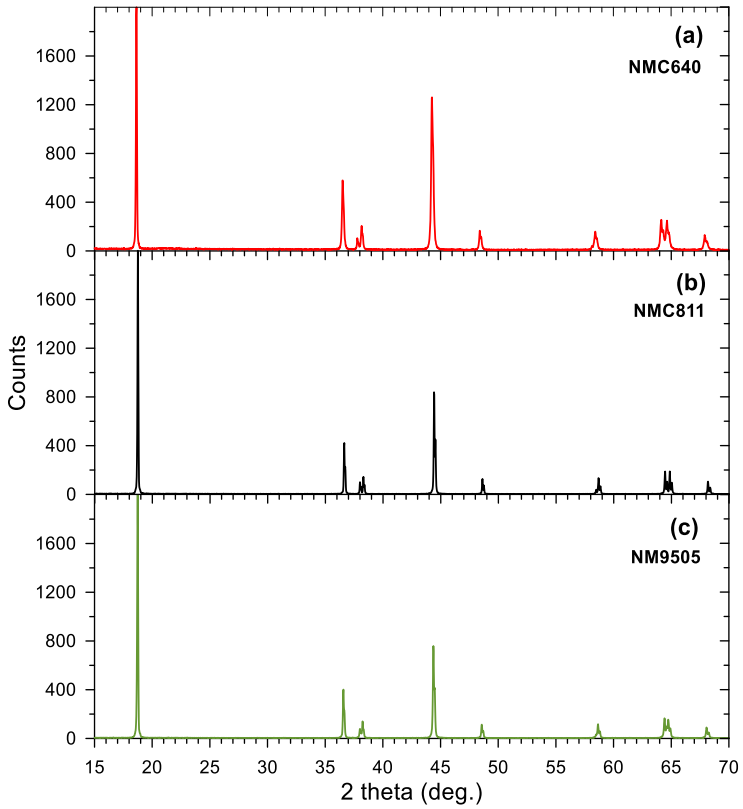

Figure 15: XRD Spectra

Table 5: Reitveld Refinement

Material	Lattice Parameter a	Error	Lattice Parameter s	Error	%Ni in Li layer	Error	Bragg R-Factor
NMC640	2.8817 Å	6.66E-5 Å	14.264 Å	5.73E-4 Å	7.45%	0.1166%	5.87
NMC811	2.8719 Å	5.78E-5 Å	14.189 Å	2.94E-4 Å	2.20%	0.1431%	3.02
NM9505	2.8766 Å	5.64E-5 Å	14.190 Å	2.81E-4 Å	1.86%	0.1183%	2.72

Chapter 7: Results and Discussion

7.1 Single Cell Example

Figure 16 shows some of the key results returned by AMIDR of a single $LiNi_{0.95}Mn_{0.05}O_2$ (NM9505) cell. Most values are plotted with the average voltage of their pulse, but R is plotted with the initial voltage of their pulse as this is primarily where R is realized. It can be immediately observed both in D and R that kinetics get continuously worse at low SOC which aligns with other studies of layered oxides.[17–21] This makes intuitive sense as it is expected that D_c would get worse with additional crowding of ions in the lattice. Kinetics get so sluggish for SOC < 3.6 V that pulses become incomplete suggesting that relaxation times are also incomplete, and the results are erroneous. This results in a lack of agreement between charge and discharge results in D_c, D_t^*, and dq/dV. R appears to still be in good agreement for SOC < 3.6 V because R does not require significant periods of time to develop or relax. There is a mild disagreement between charge and discharge R measurements at SOC 3.65 – 3.85 V which may be due to measurement error but is more likely due to cell R growing during cycling. Results for SOC > 4.15 V are erroneous for a different reason. At this SOC, dq/dV increases dramatically which is associated with the H2-H3 phase transition commonly found in high-Ni layered oxides.[22] This dramatic change in dq/dV means that pulses within this region cannot be expected to have a consistent dq/dV and therefore calculation of τ will be inaccurate. The current and relaxation times for SOC 3.6 – 4.15 V can be easily validated as these protocol parameters change at 3.7 V and there are two extra long relaxation times

at 3.7 V and 3.95 V between protocol sections, but all results appear continuous at these SOC.

D_c and dq/dV are shown to be inversely related to each other for SOC > 3.7 V. This is not coincidental as the greater difference in occupation site potential associated with low dq/dV encourages greater transport from high to low concentration regions. This inverse relationship has interesting implications regarding the calculation of D_t^* using equation 25. D_c and dq/dV cancel each other out leaving behind a relatively consistent D_t^* for SOC > 3.7 V. The derivation of D_t^* given by equation 23 suggests that the average ΔG_A is also mostly consistent within these SOC as ΔG_A is the only term that could conceivably change because of a change of SOC. This derivation could also be used to calculate the average ΔG_A if multiple tests were done at varying T, but this was not accomplished within this study. The cancelling out of this inverse relationship is also present when calculating $R_{D,term}$ using equation 13 leaving a $R_{D,term}$ that is relatively consistent for SOC > 3.7 V despite changing D_c and dq/dV. This makes sense as equation 26 shows that ΔG_A is the primary factor determining $R_{D,term}$ and, therefore, the overall long timescale kinetic performance.

It is known that a vacancy of the target occupation site is necessary for site hopping transportation to occur and this is accounted for in deriving D_t^*. However, it has also been shown that adjacent vacancies allow for a transport pathway through an intermediate tetrahedral site reducing ΔG_A. This is known as divacancy hopping and is the dominant mode of transport when available.[21] Divacancies become uncommon when the layered

oxide is more saturated at low SOC and therefore the average ΔG_A increases with further saturation in agreement with the downward trend of D_t^* for SOC < 3.7 V. Much more recently, it has also been shown that even if both adjacent occupation sites are occupied by lithium atoms, low ΔG_A site hops with similar ΔG_A to that of divacancy hops can occur if the doubly-adjacent occupation sites are vacant.[23] This particular study is still undergoing peer review, but gives a better explanation for why D_t^* is constant at SOC > 3.7 V where divacancies may still be uncommon, but doubly-adjacent occupation sites are still commonly vacant.

The benefits of using AMIDR to determine R are shown as well. A common, traditional method to measure R is to calculate it as $R = \Delta V_1/I$, where ΔV_1 is the initial change in voltage between the first two datapoints of the pulse. However, the exact value of ΔV_1 is dependent on the sampling rate selected by the user or limited by the cell tester. If the sampling rate is too fast such as measuring once every 0.05 s, R may be underestimated as the total η_R may not be fully realized due to delay from capacitive effects. If the sampling rate is too slow such as measuring once every 5 s, R may be overestimated as a significant portion of η_D will be measured with η_R. This suggests that you might have a window of accuracy with a sampling rate such as once every 0.5 s, but this just includes both errors. It can be seen that R measured with the ΔV_1 after 0.5 s is overestimated at high SOC and underestimated at low SOC. The minimum time it takes for η_R to be realized is dependent on the total amount of R, so there is no optimal sampling rate for accurately measuring all possible values of R.

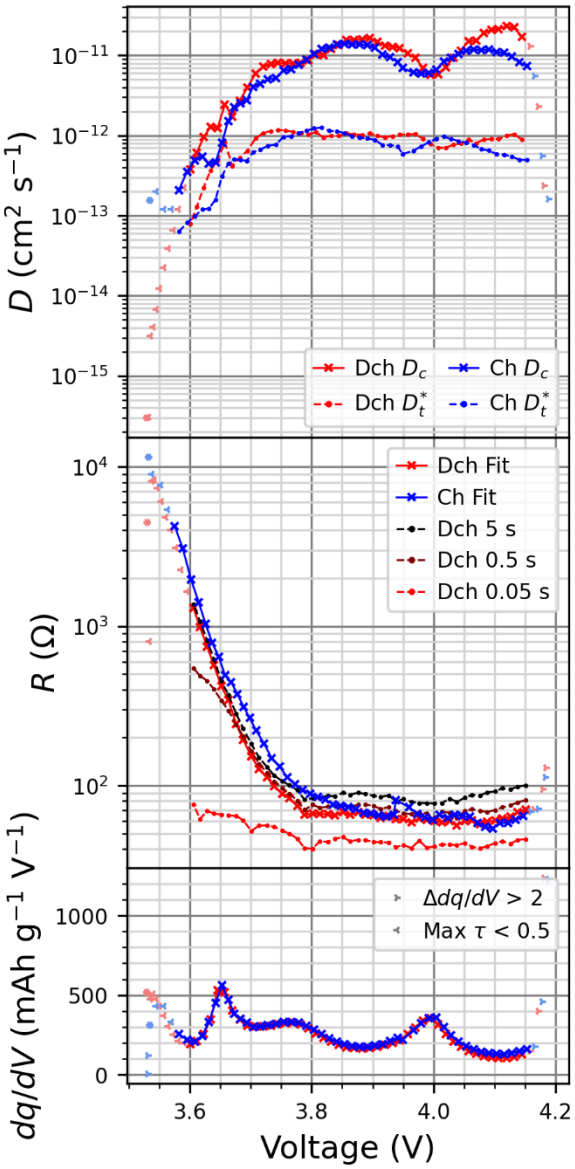

Figure 16: AMIDR results of a single NM9505 cell at 30 °C. Incomplete pulses and poor kinetics are common at low SOC and large dq/dV changes are common at the H2-H3 phase transition > 4.15 V. Chemical diffusivity, D_c, varies inversely with dq/dV leaving a relatively flat free-path tracer diffusivity, D_t^*. Resistance, R, measured from initial voltage changes is either underestimated or overestimated compared to fit R for all sampling rates. D_t^* and initial voltage change R results from erroneous pulses are not shown for clarity.

7.2 Charge/Discharge Disagreement

While charge and discharge results generally align, there is a measurable difference between the two that curiously revolves around dq/dV peaks and valleys. Figure 17a shows binned and averaged data from multiple cells using a beta protocol from early in AMIDR development. It's apparent that the calculated D_c and D_t^* values are higher when dq/dV is decreasing during a pulse and vice versa. This suggests that change in dq/dV produced error in the calculated D values. One explanation is that decreasing dq/dV gives the impression that the η_D in the middle of a pulse is smaller than it's expected to be, overestimating D_c in the fitting. The opposite would occur for increasing dq/dV and the error would be minimized for pulses upon dq/dV peaks and valleys as the dq/dV change is also minimized. Figure 17b shows data from a newer, high resolution protocol developed in response to this charge/discharge disagreement with voltage limit spacing half the size of the beta protocol. Charge/discharge disagreement is still apparent with the high resolution protocol but appears to be marginally improved.

An issue making comparison of these two datasets difficult is that the beta protocol cells were coated on a rougher than ideal surface which encouraged active material agglomeration. Unfortunately, these cells were built early in development of AMIDR before the issue of a rough coating surface was realized. This agglomeration caused groups of particles to act as larger particles giving the impression of smaller D_c with higher variance. The agglomeration produced consistently higher fit errors, even for pulses upon dq/dV peaks and valleys.

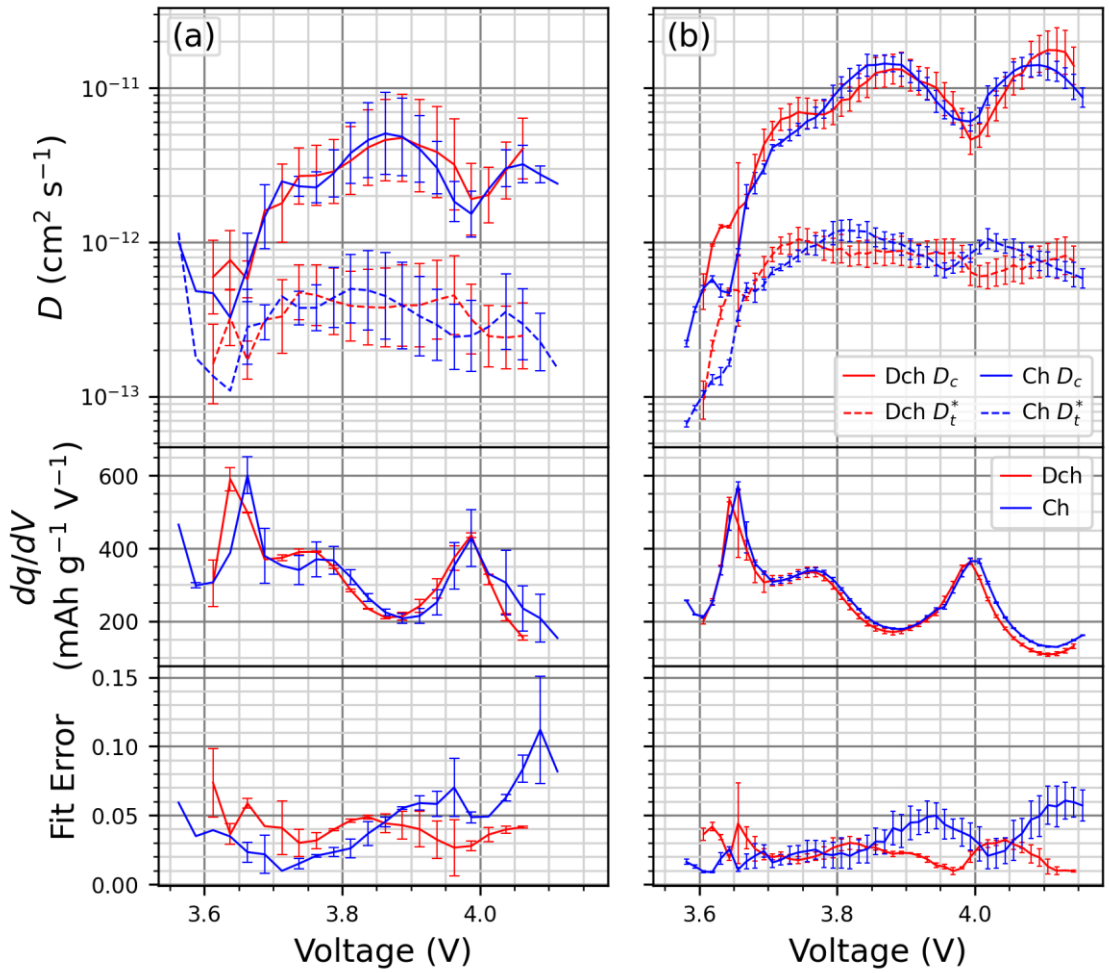

Figure 17: Comparison of NM9505 cells at 30 °C tested with (a) an early beta protocol and (b) a high resolution protocol. Additionally, the cells made for the beta protocol were coated on a rough surface and had issues with particle agglomeration. Cell data was binned into voltage ranges and averaged. Both protocols generated charge/discharge disagreement in diffusivity, D, revolving around dq/dV peaks and valleys. The high resolution protocol shows larger D values with less charge/discharge disagreement, variance, and fit error.

7.3 Counter Electrode Impact

Because charge and discharge data have opposite errors, they can be binned and averaged together to return results agnostic of current direction. Figure 18 shows averaged data from NM9505 cells with both the impedance against the reference electrode and impedance against the lithium metal anode analyzed by AMIDR. These cells had minimal

cathode mass loading to amplify the cathode impedance and to eliminate electrolyte pore impedance. However, even with amplified cathode impedance, the lithium metal anode still produced enough impedance to skew results measurably for SOC > 3.7 V where cathode impedance is small. If high accuracy is not desired, it may be acceptable to simply test 2-electrode coin cells as they are far easier to make. However, if 2-electrode coin cells are tested, it is strongly recommended to compare their results to the impedance of lithium metal symmetrical cells to ensure that it is not simply lithium metal impedance that is being measured.

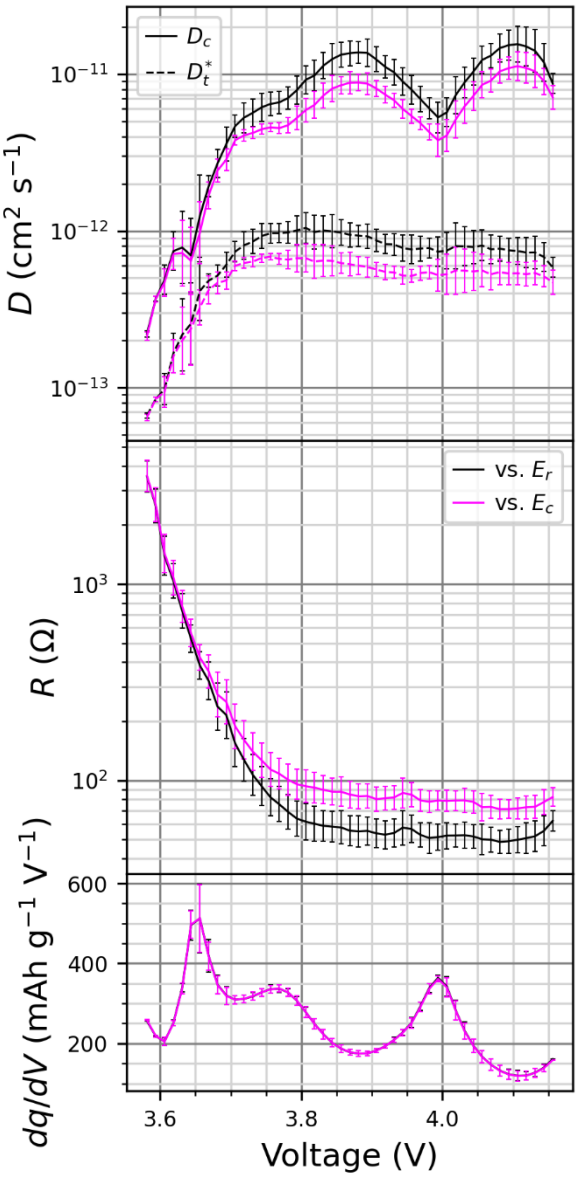

Figure 18: Comparison of NM9505 cells at 30 °C analyzed with impedance against the reference electrode potential, E_r, and impedance against the counter electrode potential, E_c. Even with minimal cathode mass loading to amplify cathode impedance, impedance from a lithium metal anode can obscure diffusivity, D, measurements.

7.4 Impact of Cell Tester

Figure 19 shows the difference between a material measured with a Novonix (NVX) UHPC 2A cell tester and a Bio-Logic (BL) VMP-3e cell tester. Both cells were

analyzed against the counter electrode potential, E_c, because at the time the NVX tests were completed the 3-electrode cells had not yet been developed. While certain differences can be attributed to the cell tester, some difference might be attributed to other changes made in the AMIDR development process between the times that these two testes were taken. The main difference between the two is the large amount of noise produced by the NVX cell tester. Figure 20 shows the source of this noise which is a noisy current initiation at the beginning of pulses. This adds error to the initial ΔV measurements which are essential for deciphering how much η is from η_R or η_D.

Additional to the use of the NVX cell tester, the cells made at that time were coated on a rough surface which introduced particle agglomeration. Secondly, the protocol used for the NVX cell tester was designed with no 0 A CC step before the pulse. It's unclear whether the NVX cell tester suffers from the same effect of undesired static charge being introduced by mechanical reconnection of the galvanometer that the BL cell tester does, but it can be seen in many of the fits produced (see Figure B7) that the Q value of the first datapoint is larger than expected suggesting a larger than expected initial ΔV. Additionally, the voltage drop R of the NVX cell tester results was higher than the fit R, which shows that the first datapoint saw a greater initial ΔV than the rest of the datapoints suggest it should have. Otherwise, while the cells on the NVX cell tester showed less D_C and more R, it's unclear exactly which differences influenced these results.

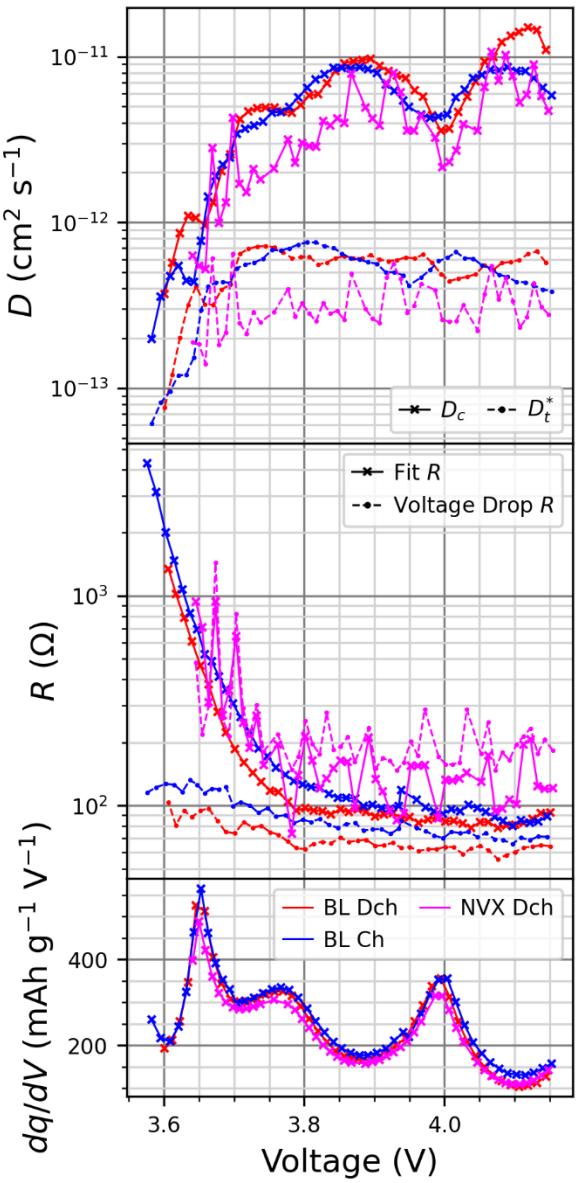

Figure 19: Comparison of NM9505 cells at 30 °C tested with Bio-Logic (BL) and Novonix (NVX) cell testers. Both cells were analyzed against the counter electrode potential, E_c. Additionally, the cells made for NVX cell testers were coated on a rough surface and had issues with particle agglomeration, and the NVX protocol was designed with no 0 A CC step before the pulse. NVX cells showed greater noise and worse resistance, R, and chemical diffusivity, D_c.

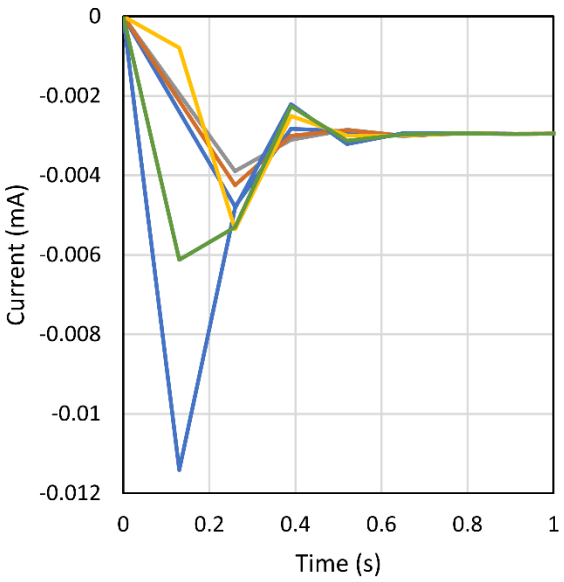

Figure 20: Low current pulse initiations from a Novonix cell tester. Each colour represents a separate pulse initiation.

7.5 AMID Comparison

Figure 21 shows AMIDR results compared to AMID results of the same material which reveals the magnitude of error in AMID. Additionally, AMID data collected with the AMID protocol is evaluated with the AMIDR model to show which steps resolved which sources of error. Firstly, AMID underestimated D measurements by somewhat less than a factor of 10 by reading η_R as η_D. Using the AMIDR model on AMID data somewhat rectified this and found D values that were generally in line with AMIDR results even despite the approximation of Δq_c as Δq which is inaccurate for high I pulses with dynamic η_D. However, with limited dynamic η_D data, AMID with the AMIDR model had trouble pinning down exactly how much η was η_D versus η_R. This is observed with the mid to high SOC fits which paired high D measurements with high R measurements and vice versa. AMIDR was able to solve this by collecting far more dynamic η_D with the single current

protocol, which also provided far greater V resolution and accuracy. This was very consequential at low SOC where D and R change rapidly. For low SOC, AMID had an interval from 3.0 – 3.6 V which we can now tell was mostly measuring η near 3.6 V as it's infeasible to access SOC near 3.0 V given the extreme η. Lastly, AMID gave results for the H2-H3 phase transition at SOC > 4.15 V. AMIDR didn't measure this region due to a longer relaxation period before discharge where side reactions reduced the starting V. The remaining pulses near the H2-H3 phase transition were removed due to rapidly changing dq/dV. It appears that AMID likely acquired error both from the high V side reactions and the rapidly changing dq/dV.

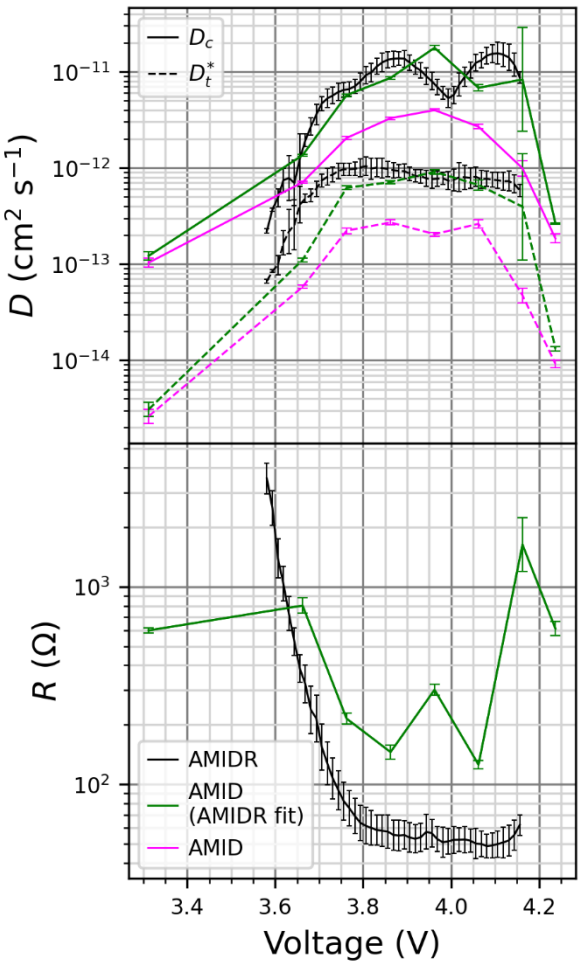

Figure 21: Comparison of NM9505 cells at 30 °C analyzed with AMIDR, AMID, and AMID data evaluated with the AMIDR model. The AMIDR model assisted in getting more accurate D measurements, whereas the AMIDR protocol improved V resolution and accuracy.

7.6 Material Comparisons

Figure 22 shows the difference in kinetics of three different types of commercial layered oxide active materials. It can be immediately seen that $LiNi_{0.8}Mn_{0.1}Co_{0.1}O_2$ (NMC811) and NM9505 have very similar kinetic performance as high-Ni layered oxides with a similar proportion of Ni in the Li layer, Ni_{Li}, determined with XRD (see Figure 15 and Table 5). D_c at the 4.0 V q-V plateau unique to NM9505 is somewhat worse than NMC811, but this q-V plateau has similar overall kinetic performance due to having a

similar D_t^* and therefore similar $R_{D,term}$. $LiNi_{0.6}Mn_{0.4}O_2$ (NMC640), however, shows much worse kinetic performance at most SOC. This is because the NMC640 has higher Ni_{Li} which prevents divacancy hops at adjacent sites. However, at low SOC where the active material has high Li saturation, NMC640 shows similar kinetic performance to the other materials as divacancies are uncommon for all materials at this SOC.

The three commercial materials also have very similar maximum ρ_c as a function of voltage. It's important to recognize this measurement as a maximum value because a certain amount of R in the cell is not sourced from the active material surface. However, R_i is the only source of R that could conceivably change with SOC, so it's fair to regard the larger values of ρ_c as effectively entirely due to R_i as other sources of R would be negligible. It's hard to determine whether R_i is primarily due to a single charge transfer reaction or a thin, low D_c surface layer as they both generate R_i independent of the currents applied. If it is a single charge transfer reaction between the electrolyte and the active material, then it would be expected to follow the Butler-Volmer equation. However, the relationship between current density, $j = I/S$, and η in the Bulter-Volmer equation is linear for $\eta < 25$ mV and no pulse had $\eta > 25$ mV as the voltage limit spacing was set at 25 mV or less. The expected charge transfer resistance, R_{ct}, would therefore follow Ohm's law and be consistent across varying I. R_i may also be due to a negligible charge transfer reaction and a thin, low D_c surface layer. Commercial active material is often engineered with surface treatments to extend cycle life and a reconstructed rock salt surface layer is often observed for layered oxides.[8] A thin surface layer can be modeled as a thin, low D_c

phase effectively producing an R_i that also follows Ohm's law on a reasonably short timescale (see Proof A3). It is possible that the observed increase in R_i during the charge pulses after the discharge pulses is due to a thickening of this surface layer. However, it's also possible that the observed increase in R_i may also be due to a decrease in active material surface area accessible to charge transfer due to the growth of an impenetrable surface layer. Regardless, it's clear that R_i is heavily dependent on SOC in a manner similar to D_c.

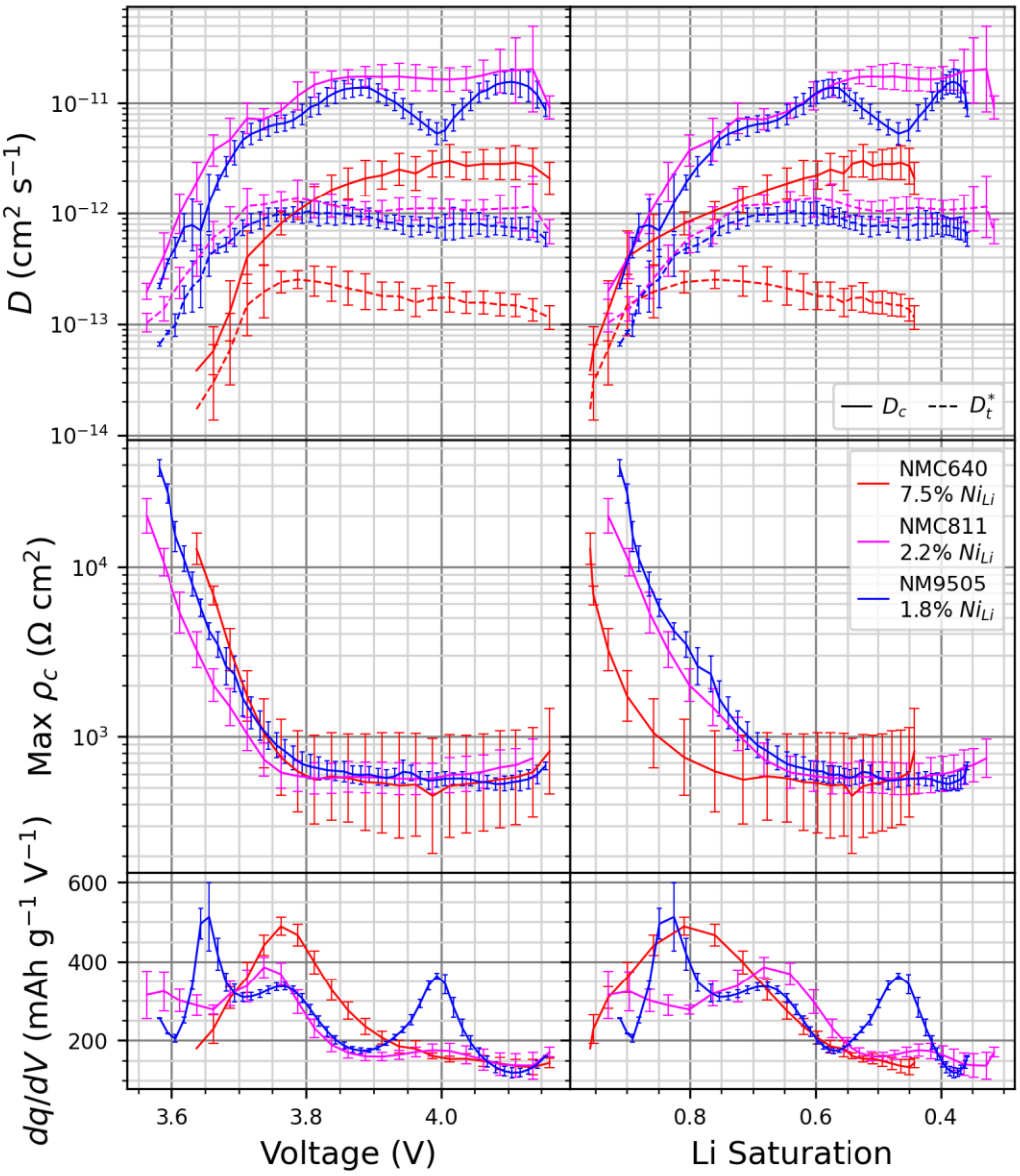

Figure 22: Comparison of commercial layered oxide materials at 30 °C. NMC811 and NM9505 show similar kinetics with similar Ni in Li layer, Ni_{Li}, measured with XRD. NMC640 has additional Ni_{Li} and worse kinetics.

Chapter 8: Dynamic Diffusivity Models

Combining equations 24 and 25 shows the complete derivation of D_c as

$$D_c(q) = \frac{zq_e a^2 \nu q \left(1 - \frac{q}{q_{sat}}\right)}{2Ck_B T \frac{dq}{dV}} e^{-\frac{\Delta G_A}{k_B T}}. \quad (27)$$

Many of these terms are consistent with changing SOC with the exception of q, $(1 - q/q_{sat})$, dq/dV, and $e^{-\Delta G_A/k_B T}$. q describes the reduction in D_c with decreasing SOC due to target occupation sites being filled and $(1 - q/q_{sat})$ describes the expected dq/dV of a dilute solute without solute-solute interaction. Both of these terms adjust minimally and gradually over the accessible SOC of the active material, so they have minimal impact upon D_c. dq/dV and ΔG_A, however, can change rapidly with a small change in SOC. The next two models will investigate how a pulse with dynamic D_c due to dynamic dq/dV and ΔG_A will behave.

8.1 Dynamic Diffusivity due to dq/dV

Within layered oxides, dq/dV may change at any SOC, especially high-Ni active material such as NM9505. It has been shown previously in the analyzed experimental data that high and low dq/dV pulses will produce the same $R_{D,term}$ and general impedance, however, this does not explain what happens when dq/dV changes significantly within a pulse. This is explored with a 1-D planar sheet, analytical, finite difference model using Fick's laws of diffusion generated in Microsoft Excel.

This model was designed with arbitrary units for simplicities sake. The planar sheet was given $r = 2$ on either side both experiencing $J = \pm 0.25$ depending on whether the active material is being charged or discharged. The most discharged state was defined as $q = 0$ with $c = 2$ corresponding to $V = -0.25$, and the most charged state was defined as $q = 2$ with $c = 0$ corresponding to $V = 4$. When $c > 1$, the active material was given $dq/dV = 4$ and $D_c = 0.25$, and when $c < 1$, the active material was given $dq/dV = 0.25$ and $D_c = 4$. This inverse relationship between dq/dV and D_c means we assume that dq/dV is the only thing that impacts D_c as you might expect within a small SOC range far above low SOC.

Figure 23a and b show the active material concentration under charge and discharge, respectively. It can be seen that when $c > 1$ the smaller D_c encourages larger concentration gradients. During charge at the transition to $c < 1$ it can be seen that the change in c_s over time slows down as the interior c changes more rapidly and the opposite is true for discharge.

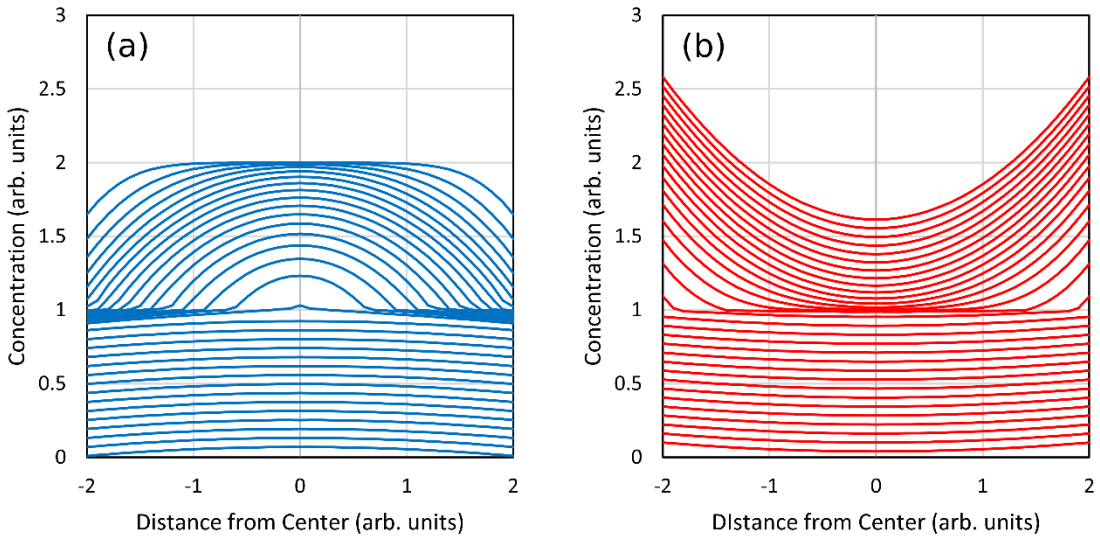

Figure 23: Internal concentration, c, of a modeled 1-D planar sheet with dynamic chemical diffusivity, D_c, under (a) charge and (b) discharge. When concentration, $c > 1$, $D_c = 0.25$, and when $c < 1$, $D_c = 4$.

Figure 24 shows the potentials of this model over capacity. It can be seen for both charge and discharge that the pulses begin with a growth of overpotential until a steady state is reached. After this, the overpotential resembles a simple resistive overpotential. However, once the $c = 1$ boundary is reached, both pulses deviate from this and a larger potential than what one might expect from a resistive overpotential is seen. It can be expected that if the dq/dV and D_c values were switched that both pulses would deviate with smaller potential. It can be seen that the diffusion overpotential generates a "blurring" of details of the dq/dV whereas a resistive overpotential would retain these details. This can be a useful trick to use when looking at high rate cycling data to determine if most impedance is sourced from diffusion or resistance. It can be seen that in the steady state portions of the pulse that the difference in potentials between charge and discharge is

consistent. The dq/dV transition region also gives this appearance, but it's unclear whether this is truly the case.

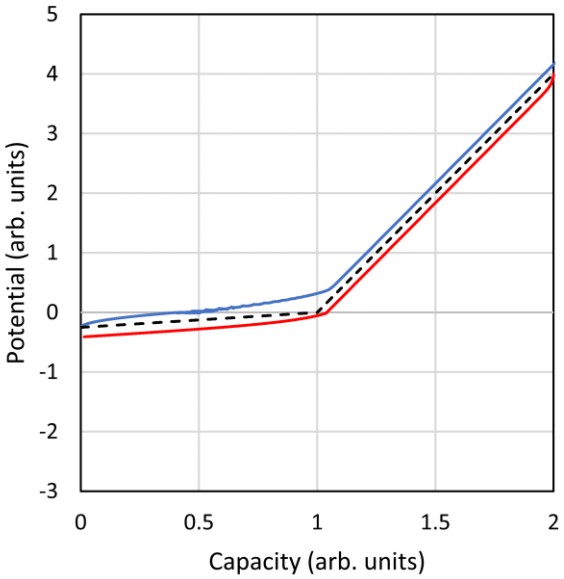

Figure 24: Voltage vs. capacity of one cycle of a modeled 1-D planar sheet with dynamic chemical diffusivity, Dc, and differential capacity, dq/dV. When concentration, $c > 1$, $dq/dV = 4$ and $D_c = 0.25$, and when $c < 1$, $dq/dV = 0.25$ and $D_c = 4$. The dashed line represents the impedance free voltage.

By chance, it was noticed that Figure 24 bears a striking resemblance to Figure 25, which features one cycle of a layered oxide, Na-ion cell. This particular Na-ion material has not yet been tested by AMIDR but could be if a Na-ion reference electrode is developed. It would not be shocking if Na layered oxides shared similar D_c profiles to Li layered oxides. The one feature that is different is the low SOC tail of the discharge pulse which is quite likely due to small D_c due to increasing ΔG_A due to elimination of divacancies.

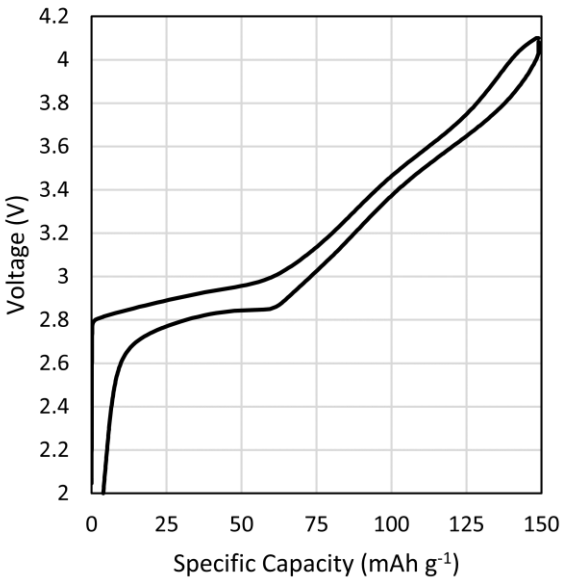

Figure 25: Voltage vs. capacity of one cycle of a layered oxide, Na-ion active material. This cell was made and tested by Libin Zhang and Bailey Rutherford.

8.2 Dynamic Diffusivity due to ΔG_A Near End of Discharge

At end of discharge, D_c shrinks due to increasing ΔG_A. This drives a higher c_s which in turn drives an even lower D_c at the surface, $D_{c,s}$. This results in a positive feedback loop that rapidly increases c_s and decreases $D_{c,s}$ leaving c in the interior of the particle relatively unchanged and resulting in a characteristic low SOC tail as seen in Figure 25 and Figure 26. This feedback loop can technically happen at any SOC where increased c_s leads to lower D_c, but it only becomes a runaway feedback loop that leads to end of discharge when there is a large difference in D_c within the particle.

At low SOC, Figure 22 shows that D_c roughly has an exponential decay relationship with q (this appears linear on a logarithmic plot). Given that these pulses begin with uniform c and c with linear with q, we can define the D_c as a function of c as

$$D_c(c) = Me^{-Nc}, \tag{28}$$

where M ($cm^2\ s^{-1}$) and N ($cm^3\ mol^{-1}$) are active material specific constants. The spatial gradient of D_c ($cm\ s^{-1}$), ∇D_c, can be calculated as

$$\nabla D_c(c) = -NMe^{-Nc}\nabla c = -ND_c(c)\nabla c. \tag{29}$$

From here, it can be helpful to express this in terms of J using Fick's first law ($J = -D_c\nabla c$) as

$$\nabla D_c(c) = NJ. \tag{30}$$

This shows that at any point along a diffusion path, the gradient of D_c is determined by simply J and the D_c rate of exponential decay in terms of c, N. This gradient may be rather significant if D_c is small, but insignificant if D_c is large. Therefore, it will be normalized by D_c to produce the relative spatial gradient of D_c (cm^{-1}), $\nabla\widetilde{D}_c$ as

$$\nabla\widetilde{D}_c(c) = \frac{NJ}{D_c(c)}. \tag{31}$$

Next, this can be localized to surface to produce the relative spatial gradient of D_c at the surface, $\nabla\widetilde{D}_{c,s}$, using $J = z^{-1}F^{-1}IS^{-1}$ as

$$\nabla\widetilde{D}_{c,s} = \frac{NI}{zFSD_{c,s}}. \tag{32}$$

When $\nabla\widetilde{D}_{c,s}$ is large, this means that D_c changes dramatically over a short distance, and when $\nabla\widetilde{D}_{c,s}$ is small, this means that D_c barely changes over a long distance. The appropriate distance to compare to is r as this will determine whether there is a significant

volume of unchanged c active material in the interior of the particle. When $\nabla\widetilde{D}_{c,s} \ll r^{-1}$, D_c throughout the particle can be treated as uniform whereas when $\nabla\widetilde{D}_{c,s} \gg r^{-1}$, the particle will have non-uniform D_c, the runaway feedback loop will have begun and end of discharge will be imminent. In equation 32, the only term that is controllable after a cell has been built is I. Therefore, it's desired that I does not ever increase above a $D_{c,s}$ dependent, critical threshold at low SOC. If the runaway feedback loop begins, $D_{c,s}$ will shrink rapidly and a reduction in I will be too late to stop it. Using equation 28, this critical threshold for I, I_c, can be defined in terms of measured V during a pulse as

$$I(V) \ll I_c(V) = \frac{zFSMe^{-Nc_s(V)}}{Nr}, \tag{33}$$

where the function for c_s in terms of V is known from relaxed potential measurements. Because measured V is dependent upon η_R as well as c_s, c_s may be overestimated and I_c underestimated, but this is fine because underestimating I_c will not cause the active material to enter the runaway feedback loop. This underestimation due to η_R will also be minimized at lower SOC and lower I_c where $\eta_D \gg \eta_R$. Figure 26 shows discharges for a series of different I and estimations placed by eye of what V initiates an end of discharge feedback loop.

Equation 33 is a particularly powerful equation because this can be used to maximize I at any given V without causing end of discharge. Simply put, by not surpassing I_c, energy density and power density can be simultaneously maximized at low SOC using a dynamic I discharge. This may not be practical for electric vehicles which require a

minimum I for use but could be very practical for eking the last bits of energy out of a stationary storage project.

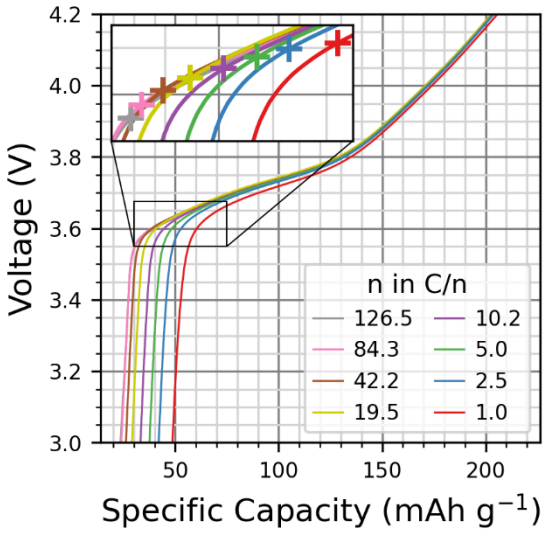

Figure 26: Voltage vs. capacity of discharges at different rates of a thin electrode, Li-ion NMC622 active material in a half cell. The '+' signs placed by eye estimate the initiation of the end of discharge feedback loop. n in C/n is the approximate number of hours it takes to discharge a cell at a given I. This cell was made and tested by Eniko Zsoldos.

Chapter 9: Conclusion

AMIDR is an improved method for measuring D_c due to a series of important design decisions that all must be considered to achieve accuracy. Notably, test cells are designed to amplify active material impedance and ignore impedance from the opposing electrode, the cell testing protocol and analysis are designed to measure complete pulses which reach a steady state, the analysis program is designed to calculate both cell R and D_c simultaneously by fitting to a complete pulse model, and extra care is taken to detect and remove erroneous outliers and achieve effective charge/discharge agreement. With careful application of this method, insight into the mechanistic construction of D_c and R_i is revealed. In addition, three different layered oxide materials were analyzed, and their results compared giving further evidence that layered oxide D_c is heavily dependent on Ni_{Li}, but not necessarily at low SOC. Lastly, the impact to the voltage response of pulses with variance in D_c was investigated in dynamic D_c models to connect AMIDR results to the behaviour of cells cycling over the entire SOC.

9.1 Future Work

While AMIDR is in a complete form capable of use, this does not mean that it cannot be developed further. There are many possible improvements that can be made and active materials that have not yet been explored.

Firstly, the 3-electrode coin cell assembly process has a high failure rate and is relatively labour intensive. Improvements could be made to improve both of these. Reducing thickness of the internal components may be a way to reduce pressure upon the Au wire between the cap and the gasket where the wire is often clipped off. The stripping has traditionally been mechanically done with a scalpel which is the most labour intensive step in building these cells. But it has also been recommended in conversation by the members of the lab that initially designed this process that chemical stripping with concentrated KOH will also work. However, the paper referenced in this conversation claims that the wire was stripped mechanically with a scalpel.[24] Clearly, this should at least be investigated.

Secondly, AMIDR is not yet able to measure Na-ion or K-ion active materials. This is because a Na-ion or K-ion coin cell reference electrode has not yet been developed at this lab. However, the same lab that developed the Au wire Li reference electrode used in AMIDR has also developed a tinned Cu Na reference electrode.[25]

Thirdly, while D_t^* is a useful measurement for understanding the trends of ΔG_A, ΔG_A can actually be strictly calculated using equation 24 by running AMIDR on active material

at 2 or more different temperatures. This will also inform us of ν which is admittedly not as exciting but still useful for validating results.

Fourthly, it would be valuable to better measure high dq/dV regions which AMIDR struggles with. Better measuring high dq/dV regions would allow AMIDR to measure high-Ni materials with plateaus associated with quick but continuous phase transitions. These regions require much smaller voltage limit spacing and therefore better voltage resolution measurements. Smaller voltage limit spacing will also require smaller currents to achieve complete pulses. However, the reduced D_c due to increased dq/dV also means that these pulses would take a longer period of time to develop and therefore, perhaps not require as high of a sampling rate. In this case, a different cell tester may be valuable. Regardless, work could be done to bring up AMIDR on different cell testers anyway, because this would expand flexibility and the number of tests that could be done simultaneously.

Fifthly, it would be even more valuable to measure high dq/dV regions associated with discrete phase transitions found in materials like LFP/LMFP and LMO. However, this may be very challenging. The existence of these discrete phase transitions suggests a D_c of 0 according to equation 21. However, the phase transitions being discrete also means that the region of phase transition is theoretically infinitesimally thin. This intuitively suggests that the impedance of the phase transition may be better modeled by something like the Butler-Volmer equation for discrete, single step, charge transfer reactions. However, the surface defining the discrete phase transition exists at a dynamic position within a material

in series with impedance from a non-uniform diffusivity. The equations within this study are certainly not adequate for modeling such a complex system.

Lastly, while there is now a method to calculate I_c with AMIDR, this method has not yet been tested with an actual cell. AMIDR could be used to evaluate the V and D_c profile of an active material, and those results could be used to develop a protocol which always maintains a I below I_c. Then, this protocol could be tested and compared to other protocols such as a protocol ending with a constant voltage hold at end of discharge voltage. This may even be accomplished with a standard high-loading, 2-electrode cell as the low SOC η_D is large enough to drown out any other sources of impedance and only low SOC D_c is necessary to calculate I_c. Alternatively, this could be developed for an anode material to enable optimized fast charging.

Hopefully, with proper documentation, AMIDR can be further developed, and its uses further explored by future students.

Appendix A: Proofs

Proof A1: Start of Pulse Bound for an Ensemble of Geometries with Varying Diffusion Length

For pulses that stop near their start, flux is uniform for both small and large geometries. Using equation 6 and the definitions $Q = \Delta q_{tot} I^{-1} D_c r^{-2}$ and $\tau = \Delta q / \Delta q_{tot}$ returns an equation for calculating the Δq_{tot} for a single geometry that has stopped its pulse near its start,

$$\Delta q_{tot} = \frac{2r\sqrt{I\Delta q}}{A\sqrt{\pi D_c}}. \tag{A1}$$

Accordingly, the Δq_{tot} for multiple geometries that have stopped their pulse near its start is calculated as

$$\Delta q_{tot} = \sum \Delta q_{tot,j} = \sum \left(\frac{2r_j\sqrt{I_j \Delta q_j}}{A\sqrt{\pi D_c}} \right) = \frac{2\sum r_j \sqrt{I_j \Delta q_j}}{A\sqrt{\pi D_c}}. \tag{A2}$$

where the j subscript is given for individual geometries. As flux is uniform near the start of a pulse, the I_j and Δq_j per geometry is proportional to a geometry's S_j, and therefore a geometry's r_j^2 as

$$I_j = \frac{IS_j}{\sum S_j} = \frac{Ir_j^2}{\sum r_j^2}, \text{ and} \tag{A3}$$

$$\Delta q_j = I_j \Delta t = \frac{I \Delta t r_j^2}{\sum r_j^2} = \frac{\Delta q r_j^2}{\sum r_j^2}. \tag{A4}$$

Entering these into equation A2 gives

$$\Delta q_{tot} = \frac{2\sqrt{I\Delta q}\sum r_j^3}{A\sqrt{\pi D_c}\sum r_j^2}. \tag{A5}$$

Defining $\bar{r}_s = \sum r_j^3 / \sum r_j^2$ returns equation A1. Therefore, $\bar{r}_s$ averaged in this manner will accurately define the bound for pulses that stop near the start of the pulse.

Proof A2: End of Pulse Bound for an Ensemble of Geometries with Varying Diffusion Length

For pulses that stop near their end, flux is proportional to a geometry's $\tilde{V}/S$. Using equation 7 and the definitions $Q = \Delta q_{tot} I^{-1} D_c r^{-2}$ and $\tau = \Delta q / \Delta q_{tot}$ returns an equation for calculating the Δq_{tot} for a single geometry that has stopped its pulse near its end,

$$\Delta q_{tot} = \Delta q + \frac{Ir^2}{ABD_c}. \tag{A6}$$

Accordingly, the Δq_{tot} for multiple geometries that have stopped their pulse near its end is calculated as

$$\Delta q_{tot} = \sum \Delta q_{tot,j} = \sum \left(\Delta q_j + \frac{I_j r_j^2}{ABD_c} \right) = \Delta q + \frac{\sum I_j r_j^2}{ABD_c}. \tag{A7}$$

where the j subscript is given for individual geometries. As flux is proportional to a geometry's $\tilde{V}/S$ near the end of a pulse, the I_j per geometry is proportional to a geometry's $\tilde{V}_j$, and therefore a geometry's r_j^3 as

$$I_j = \frac{I\tilde{V}_j}{\sum \tilde{V}_j} = \frac{Ir_j^3}{\sum r_j^3}. \tag{A8}$$

Entering this into equation A7 gives

$$\Delta q_{tot} = \Delta q + \frac{I \sum r_j^5}{ABD \sum r_j^3}. \tag{A9}$$

Defining $\bar{r}_e = \left(\sum r_j^5 / \sum r_j^3\right)^{1/2}$ returns equation A6. Therefore, $\bar{r}_e$ averaged in this manner will accurately define the bound for pulses that stop near the end of the pulse.

Proof A3: Impedance of a Thin, Low Diffusivity Surface Layer

Taking the derivative of 1 in terms of y returns

$$\frac{dX(\tau)}{dy} = \frac{1}{AQ}\left(y - 2\sum_{i=1}^{\infty} \frac{e^{-\alpha_i^2 Q\tau}}{\alpha_i^2} \frac{dC(\alpha_i, y)}{dy}\right), \tag{A10}$$

where the ascending, non-zero series α_i and function $C(\alpha_i, y)$ is defined for each geometry as

Planar Sheet: $\sin(\alpha) = 0\ \{\alpha_1 = \pi, \alpha_2 = 2\pi, \dots\}$,

$$\frac{dC(\alpha, y)}{dy} = -\frac{\alpha \sin(\alpha y)}{\cos(\alpha)},$$

Cylinder: $J_1(\alpha) = 0$,

$$\frac{dC(\alpha, y)}{dy} = -\frac{\alpha J_1(\alpha y)}{J_0(\alpha)},$$

Sphere: $\alpha\cot(\alpha) - 1 = 0$,

$$\frac{dC(\alpha, y)}{dy} = \frac{\alpha y \cos(\alpha y) - \sin(\alpha y)}{y^2 \sin(\alpha)}.$$

Next, the derivative of X in terms of y near the surface is calculated as

$$\lim_{y\to 1} \frac{dX(\tau)}{dy} = \frac{1}{AQ}\left(1 - 2\sum_{i=1}^{\infty} \frac{e^{-\alpha_i^2 Q\tau}}{\alpha_i^2} \lim_{y\to 1} \frac{dC(\alpha_i, y)}{dy}\right), \tag{A11}$$

where the ascending, non-zero series α_i and function $C(\alpha_i, y)$ is defined for each geometry as

Planar Sheet: $\sin(\alpha) = 0\ \{\alpha_1 = \pi, \alpha_2 = 2\pi, \dots\},$

$$\lim_{y\to 1}\frac{dC(\alpha_i, y)}{dy} = -\alpha\tan(\alpha) = 0,$$

Cylinder: $$J_1(\alpha) = 0,$$

$$\lim_{y\to 1}\frac{dC(\alpha_i, y)}{dy} = -\frac{\alpha J_1(\alpha)}{J_0(\alpha)} = 0,$$

Sphere: $$\alpha\cot(\alpha) - 1 = 0,$$

$$\lim_{y\to 1}\frac{dC(\alpha_i, y)}{dy} = \alpha\cot(\alpha) - 1 = 0.$$

Conveniently, under these specific conditions $\lim_{y\to 1}\frac{dC(\alpha_i,y)}{dy} = 0$ for all geometries. This shows that the change in concentration over diffusion path position near the surface is always simply

$$\lim_{y\to 1}\frac{dX}{dy} = \frac{1}{AQ}, \tag{A12}$$

for all geometries and all τ. This equation being true for all τ is essential for a thin, low D_c surface layer to act as a resistor independent of time.

A thin, low D_c surface layer will generate a relative change in surface concentration, $X_{s,l}$, in addition to the X_s related to the bulk diffusion of the active material. As long as this surface layer is thin enough, $X_{s,l} = \lim_{z\to 1}\frac{dX}{dy}H = \frac{H}{AQ}$ where $H = h/r$ is the relative thickness and h is the thickness (cm) of the surface layer. This can be converted out of dimension-less convention to generate a change in surface concentration at the surface layer, $\Delta c_{s,l}$, as

$$\Delta c_{s,l} = \frac{Irh}{AzF\tilde{V}D_c}. \tag{A13}$$

Next, this can be converted into a surface layer overpotential, η_l, using dE/dc of the surface layer as

$$\eta_l = -\frac{dE}{dc}\frac{Irh}{AzF\tilde{V}D_c}. \tag{A14}$$

where positive I is now treated as current driving positive ions to leave the active material, the typical convention for working electrodes. Finally, this overpotential can be treated as a resistor given $V = IR$ to give a surface layer resistance, R_l, as

$$R_l = -\frac{dE}{dc}\frac{rh}{AzF\tilde{V}D_c}. \tag{A15}$$

Similar to equation 13, this is dependent on both dE/dc and D_c which will be unique to the phase of the surface layer.

Appendix B: Intermediate Analysis Results

Figure B1 shows an example of a plot that AMIDR first produces after combination of test files from individual protocols. If a test file has been forgotten to be included, it will be apparent in this plot. In addition, AMIDR also produces the plots shown in Figure B2 which show the relaxed potentials of cells undergoing AMIDR in terms of charge vs. discharge. While some cells showed better matching than others, all these cells were considered acceptable.

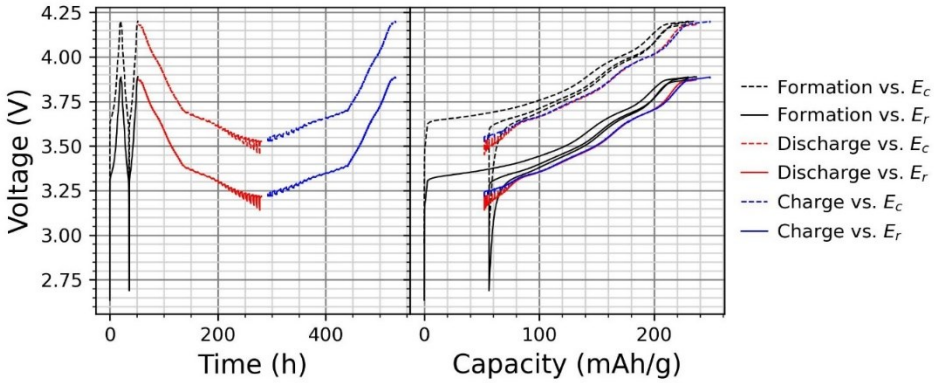

Figure B1: Example of complete test summary of a single cell.

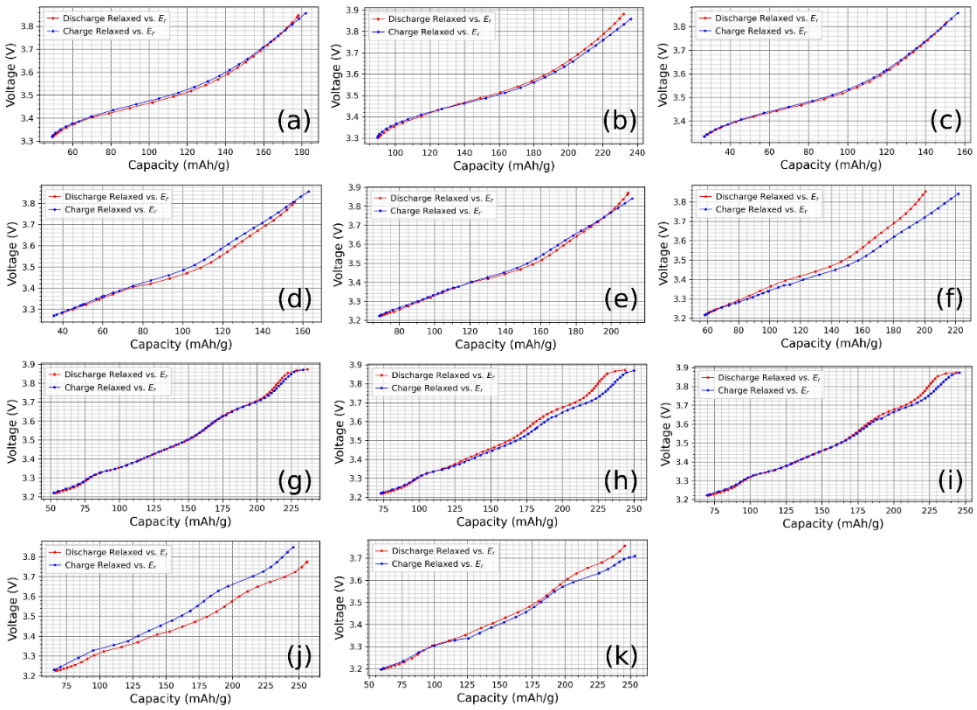

Figure B2: Matching charge vs. discharge relaxed potentials of (a-c) NMC640, (d-f) NMC811, (g-i) NM9505 with high resolution protocol, and (j-k) NM9505 with beta protocol.

Figure B3 shows fits that were removed due to having too much change in dq/dV and Figure B4 shows fits that were removed due to having too little τ. Out of the remaining fits, Figure B5 shows those with the worst fit error and Figure B6 shows a random sample. Some of the fits with too little τ may look acceptable, however, they began when the active material was not completely relaxed. The worst fitting acceptable fits are not perfect, but they are close enough to give reasonable results.

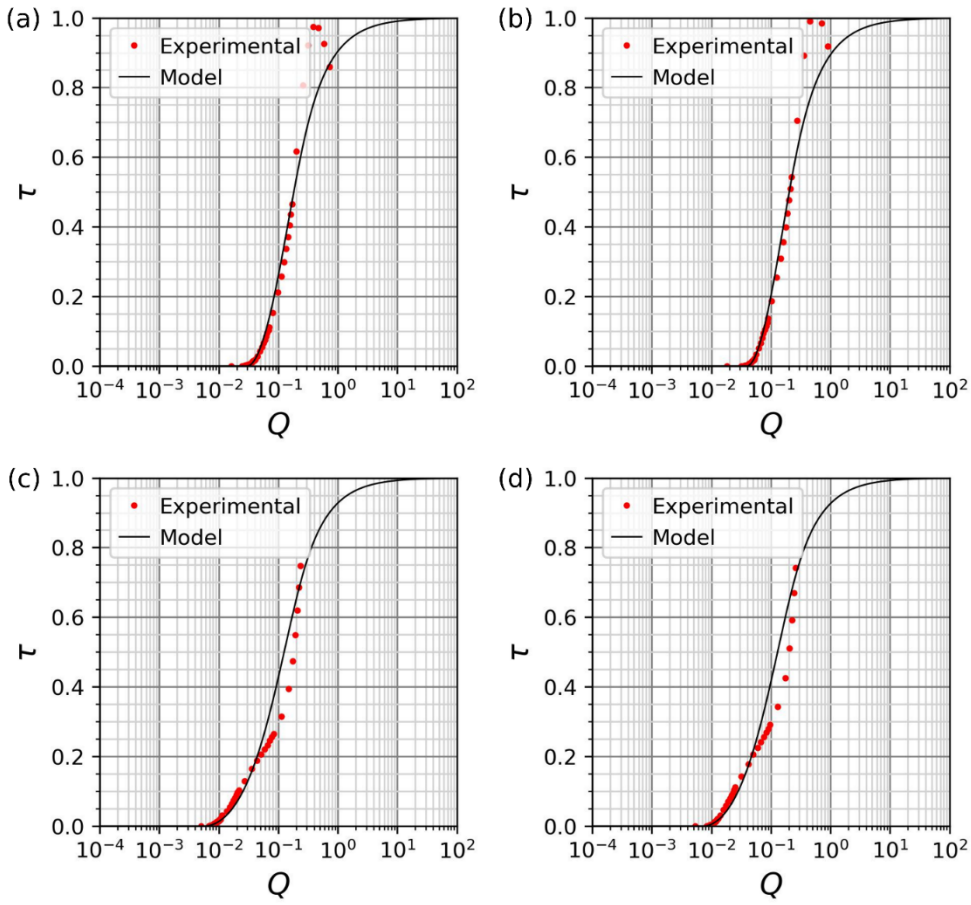

Figure B3: Examples of fits with (a-b) too much decrease in dq/dV in discharge and (c-d) too much increase in dq/dV in charge. Only NM9505 showed this error at its 4.15 V q-V plateau.

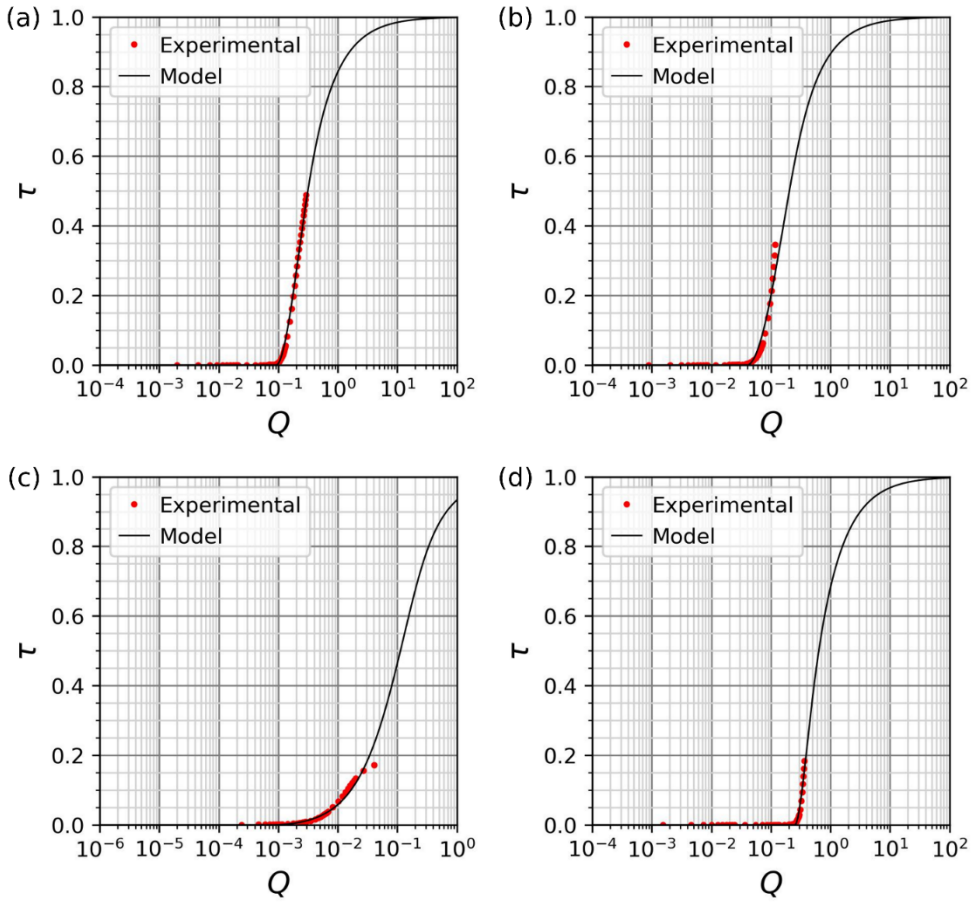

Figure B4: Examples of fits with not enough τ in order of decreasing τ. This occurs in (a, c) discharge and (b, d) charge. All cells show this error at low SOC.

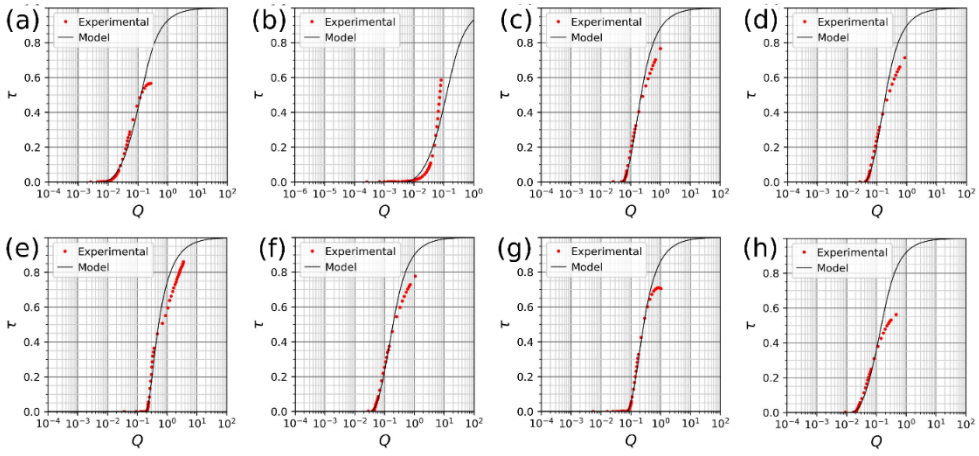

Figure B5: Examples of the highest fit error fits out of acceptable fits for (a-b) NMC640, (c-d) NMC811, (e-f) NM9505 with high resolution protocol, and (g-h) NM9505 with beta protocol. Both (a,c,e,g) discharge and (b, d, f, h) charge fits are shown.

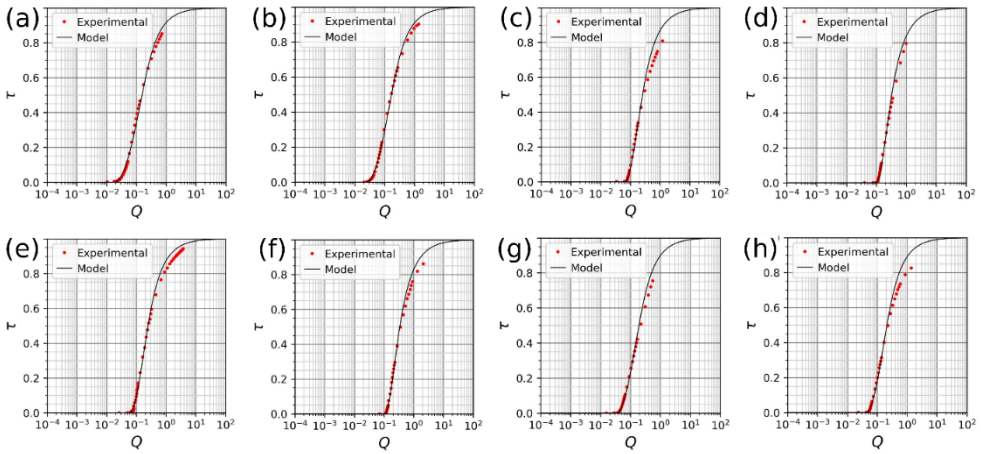

Figure B6: Examples of randomly selected, acceptable fits for (a-b) NMC640, (c-d) NMC811, (e-f) NM9505 with high resolution protocol, and (g-h) NM9505 with beta protocol. Both (a,c,e,g) discharge and (b, d, f, h) charge fits are shown.

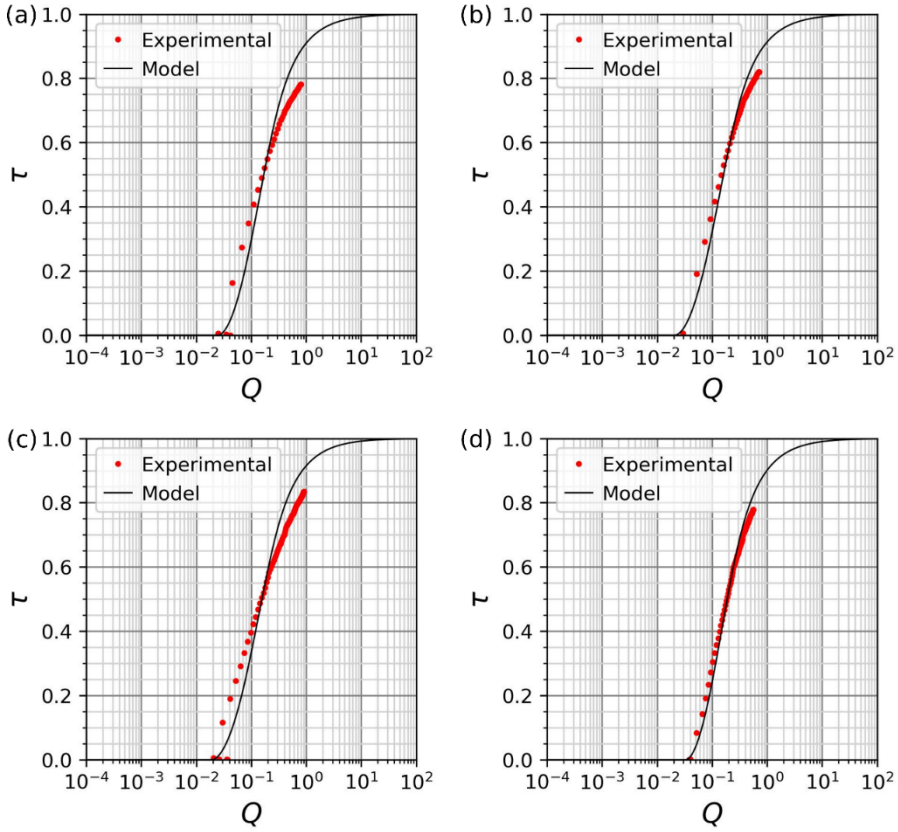

Figure B7: Examples of fits taken from a Novonix (NVX) cell tester. It can be seen that the first datapoints near $\tau = 0$ deviate significantly from the model and their Q appears overestimated.

Bibliography

1. S. Atlung, K. West, and T. Jacobsen, *J. Electrochem. Soc.*, **126**, 1311–1321 (1979).

2. S. D. Kang and W. C. Chueh, *J. Electrochem. Soc.*, **168**, 120504 (2021).

3. T. Marks, S. Trussler, A. J. Smith, D. Xiong, and J. R. Dahn, *J. Electrochem. Soc.*, **158**, A51 (2011).

4. S. Solchenbach, D. Pritzl, E. J. Y. Kong, J. Landesfeind, and H. A. Gasteiger, *J. Electrochem. Soc.*, **163**, A2265–A2272 (2016).

5. C. Liu, Z. G. Neale, and G. Cao, *Materials Today*, **19**, 109–123 (2016).

6. P. Li, H. Kim, S.-T. Myung, and Y.-K. Sun, *Energy Storage Materials*, **35**, 550–576 (2021).

7. R. Jung, M. Metzger, F. Maglia, C. Stinner, and H. A. Gasteiger, *J. Electrochem. Soc.*, **164**, A1361–A1377 (2017).

8. F. Lin, I. M. Markus, D. Nordlund, T.-C. Weng, M. D. Asta, H. L. Xin, and M. M. Doeff, *Nat Commun*, **5**, 3529 (2014).

9. C. Deng and W. Lu, *Journal of Power Sources*, **473**, 228613 (2020).

10. B. Choudhury, A. Jangale, and B. Suthar, *J. Electrochem. Soc.*, **170**, 070519 (2023).

11. H. H. Berger, *J. Electrochem. Soc.*, **119**, 507 (1972).

12. O. J. Kleppa, *Annu. Rev. Phys. Chem.*, **6**, 119–140 (1955).

13. Y. Fujihara and T. Kobayashi, *J. Electrochem. Soc.*, **169**, 080509 (2022).

14. M. Doyle, J. Newman, and J. Reimers, *Journal of Power Sources*, **52**, 211–216 (1994).

15. Y.-C. Chien, D. Brandell, and M. J. Lacey, *Chem. Commun.*, **58**, 705–708 (2022).

16. J. Kim, S. Park, S. Hwang, and W.-S. Yoon, *J. Electrochem. Sci. Technol*, **13**, 19–31 (2022).

17. A. Liu, N. Phattharasupakun, M. M. E. Cormier, E. Zsoldos, N. Zhang, E. Lyle, P. Arab, M. Sawangphruk, and J. R. Dahn, *J. Electrochem. Soc.*, **168**, 070503 (2021).

18. E. S. Zsoldos, M. M. E. Cormier, M. Ball, D. Rathore, and J. R. Dahn, *J. Electrochem. Soc.*, **170**, 070502 (2023).

19. E. Zsoldos, M. M. E. Cormier, N. Phattharasupakun, A. Liu, and J. R. Dahn, *J. Electrochem. Soc.*, **170**, 040511 (2023).

20. Y.-C. Chien, H. Liu, A. S. Menon, W. R. Brant, D. Brandell, and M. J. Lacey, *Nat Commun*, **14**, 2289 (2023).

21. A. Van Der Ven and G. Ceder, *Journal of Power Sources*, **97–98**, 529–531 (2001).

22. J. Chen, H. Yang, T. Li, C. Liu, H. Tong, J. Chen, Z. Liu, L. Xia, Z. Chen, J. Duan, and L. Li, *Front. Chem.*, **7**, 500 (2019).

23. P. Xiao, N. Zhang, H. S. Perez, and M. Park, (2023) https://arxiv.org/abs/2311.06140.

24. C. Sedlmeier, R. Schuster, C. Schramm, and H. A. Gasteiger, *J. Electrochem. Soc.*, **170**, 030536 (2023).

25. F. Linsenmann, D. Pritzl, and H. A. Gasteiger, *J. Electrochem. Soc.*, **166**, A3668–A3674 (2019).